Three-Dimensional Aeromechanical Analysis of Lift Offset Coaxial Rotors: A Helios Test Case

Mrinalgouda Patil* and Anubhav Datta†
University of Maryland, College Park, Maryland 20742

https://doi.org/10.2514/1.C036891

Three-dimensional (3-D) solid finite element analysis (FEA) is used to model and study coaxial helicopter rotors. The 3-D FEA is coupled with a lifting line aerodynamic model with free wake to capture rotor-rotor interactions. Two open-access models are developed: one is the Metaltail (a hingeless coaxial rotorcraft), and the other is the coaxial rotor built from articulated UH-60A-like rotors. The former is the main focus of this work and is developed as an example case for the U.S. Army/DoD rotorcraft simulation software CREATE™–AV Helios, while the latter is merely for a regression test. The analysis is performed on a low-speed transition flight for which qualitative data are available for the Sikorsky S-97 Raider aircraft for comparison. Predictions of performance, airloads, vibratory loads, and 3-D stresses are discussed. In the absence of available geometry or property data of the S-97, this study is primarily meant to serve as a capability demonstration of 3-D rotor structural dynamic modeling for such rotors.

Nomenclature

A	=	rotor disk area, πR^2, ft^2 (m^2)
a	=	speed of sound, m/s
C_{M_X}	=	hub roll moment coefficient
C_{M_Y}	=	hub pitch moment coefficient
C_Q	=	torque coefficient
C_T	=	thrust coefficient
C_X	=	propulsive force coefficient
c	=	chord, ft (m)
D	=	rotor diameter, ft (m)
F_X	=	hub longitudinal shear force, N
F_Y	=	hub lateral shear force, N
F_Z	=	hub vertical shear force, N
L/D_e	=	rotor lift-to-drag ratio
LO	=	lift offset, ft (m)
M^2c_n	=	sectional normal force normalized by $(1/2)\rho a^2 c$
M_X	=	hub roll moment, $\mathrm{N\cdot m}$
M_Y	=	hub pitch moment, $\mathrm{N\cdot m}$
M_Z	=	hub yaw moment, $\mathrm{N\cdot m}$
N_b	=	number of blades
R	=	rotor radius, ft (m)
z	=	rotor separation distance, ft (m)
α	=	shaft tilt angle (positive into flow), °
θ_0	=	collective, °
θ_{1c}	=	lateral cyclic, °
θ_{1s}	=	longitudinal cyclic, °
μ	=	rotor tip speed ratio
ρ	=	air density, $\mathrm{kg/m^3}$
σ	=	rotor solidity
σ_{11}	=	axial stress, $\mathrm{N/m^2}$
ψ	=	blade azimuth angle, °
Ω	=	rotor rotation speed, rad/s

Superscripts

CCW	=	counterclockwise
CW	=	clockwise
L	=	lower rotor
U	=	upper rotor

Presented as Paper 2022-0928 at the AIAA SciTech 2022 Forum, San Diego, CA, January 3–February 7, 2022; received 16 February 2022; revision received 13 November 2023; accepted for publication 20 November 2023; published online 5 January 2024.

*Postdoctoral Research Associate, Aerospace Engineering; mpatil@umd.edu (Corresponding Author).

†Associate Professor, Aerospace Engineering. Associate Fellow AIAA.

I. Introduction

THIS paper applies three-dimensional (3-D) solid finite element analysis (FEA) structural modeling to study the aeromechanics of a coaxial rotor system. This is a departure from the current state-of-the-art, where one-dimensional (1D) beam-based rotor structural models are used. A large-scale 3-D structural solver is a special-purpose high-fidelity tool envisioned for modeling new and advanced rotor blades with material and geometric discontinuities and predicting dynamic stresses and strains from first principles. The University of Maryland/U.S. Army X3D is this 3-D solver. It is refined and extended to model coaxial rotors in this work. An open-access model, Metaltail—a hingeless coaxial rotorcraft—is developed for the U.S. Army/DoD rotorcraft simulation software CREATE™–AV Helios [1] and studied as the test case here. The 3-D model of Metaltail is developed using Computer Aided Three-Dimensional Interactive Application (CATIA) and meshed in Cubit [2]. A lifting line aerodynamic model with free wake is used along with lift offset trim solution for aeromechanical analysis. Predictions of performance, airloads, vibratory hub loads, and 3-D stress fields are presented. This paper is not intended as a validation of the 3-D structural modeling; rather, it is intended as a demonstration of its capability.

A. Background and Motivation

Achieving high speed without compromising hover efficiency has been an enduring quest for rotary-wing aircraft. The high speed performance of conventional helicopters is significantly limited by vibration from compressibility on the advancing blades and depletion of propulsive force while achieving net zero roll moment at the hub. Coaxial rotors with lift offset allow roll moments in individual rotor hubs while still achieving net zero roll moment. This provides substantial benefits in speed. Moreover, their natural ability to balance torque saves tail rotor power. Interference in hover also provides 5–8% benefit in induced power relative to the single rotor with twice the number of blades [3,4]. All of these benefits come at the price of roll moment at the hub leading to high vibratory stresses and strains, which lead to heavy weight and in turn cut into performance.

The lift offset concept was demonstrated by the XH-59A demonstrator aircraft during the 1970s [5,6]. While proving basic viability, the XH-59A was compromised by aerodynamic and structural dynamic factors ranging from a heavy hub to high vibration. With renewed emphasis on high-speed rotorcraft, coaxial rotors equipped with advanced materials and cleaner hubs are being developed. The

Sikorsky X2 technology demonstrator [7,8] and S-97 Raider [9–11] are examples.

Lift offset coaxial helicopters absorb high roll moments with stiff and heavy hingeless blades, instead of traditional high flapping articulated blades. This keeps the rotor spacing to a minimum. Lift offset quantifies the roll moment as a thrust offset from the hub center. It is defined as

$$LO = \frac{|C^U_{M_X}| + |C^L_{M_X}|}{C^U_T + C^L_T} \tag{1}$$

where $|C^U_{M_X}|$ and $|C^L_{M_X}|$ are the hub roll moment magnitudes of the upper and lower rotors respectively, and C^U_T, C^L_T are thrust coefficients. The magnitude of the roll moment is taken since their signs are opposite, and nominally they cancel to achieve a net-zero roll. This is represented in Fig. 1. The lift offset (LO) is typically represented as a percentage of the rotor radius. The greater the lift offset, the higher the speed, but also the higher the loads. Absorbing higher loads either needs more motion, which leads to blade strike, or more stiffness, which leads to greater stress/strains and more weight. The hubs of modern coaxial helicopters scale drastically with gross weight—SB-1 Defiant has a much bigger hub than the S-97 Raider. These hubs need more stiffness, leading to greater hub stress/strains and more weight, impacting the vehicle's performance. The conventional beam models are sufficient to study the performance, airloads, and stability of rotors. However, they cannot capture the high stresses and strains encountered in hubs as modern rotorcraft pushes their limits in speed and range. Hence, 3-D modeling is critical. The lift offset coaxial-which pushes the boundaries of speed-is an excellent test case for this purpose.

An authoritative review of the principal works on coaxial rotors was given in 1997 by Coleman [12]. Escobar et al. [13] provide a review of the work thereafter. Some of the principal works carried out on coaxial rotor analysis are mentioned here for completeness. Modern coaxial analysis can be classified into three groups: 1) isolated computational fluid dynamics (CFD); 2) lower-fidelity lifting-line aerodynamics coupled with finite-element structural dynamics and rotor trim [called comprehensive analysis (CA)]; and 3) coupled CFD with structural dynamics and trim solution of CA (called CFD/CA coupling). The key developments of isolated CFD for coaxial rotors over the past decade are described by Ruzicka and Strawn [14], Lakshminarayan and Baeder [15], Juhasz et al. [16], Reed and Egolf [17], Seokkwan et al. [18], and Barbely et al. [19]. Isolated CFD is adequate for hover but insufficient for forward flight, where coupling with structural dynamics and trim solution is essential for any meaningful solution. Coaxial analysis with lifting-line aerodynamic models provides satisfactory predictions at low-speed forward flight. The key works using this methodology include those of Johnson [20], Yeo and Johnson [21], Schamus and Chopra [22], Cameron et al. [23], Uehara et al. [24], Feil et al. [25], Feil and Hajek [26], and Ho and Yeo [27]. In addition to these, there have been many innovative efforts to capture the coaxial wake; interested readers can refer to the works of Bagai and Leishman [28], Syal and Leishman [29], Brown [30], and Singh and Friedmann [31,32]. Coupling comprehensive analysis with CFD is a relatively new development in rotorcraft and has matured significantly for coaxial rotor applications over the last decade. It is known that the CFD/CA coupling provides the highest-fidelity aerodynamic solution for performance, loads, and vibration at high speed. Several studies have used CFD/CA on the modern coaxial rotors: Singh et al. [33] for isolated rotors; Passe et al. [34] for rotor and fuselage; Klimchenko and Baeder [35] for rotor, fuselage, and pusher propeller; and Zhao et al. [9,11] for full S-97 aircraft. This paper is not focused on predicting high-fidelity air loads but on predicting 3-D stresses and strains. As such, unsteady lifting line aerodynamic models have been used instead of higher-fidelity computational fluid dynamics.

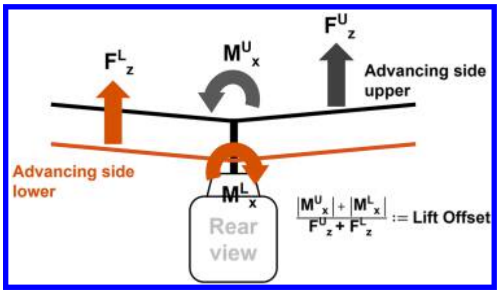

Fig. 1 Definition of lift offset for a coaxial rotor.

The NASA report by Johnson and Datta [36] identified the requirements for next-generation comprehensive analysis of rotorcraft. The future rotorcraft analysis is driven by one single CAD, and the aircraft description is obtained from this CAD system for exact aircraft representations. The subsystems—aerodynamics, structures, engine, and flight dynamics—will involve models that take information from the CAD for their respective analysis. For rotor structures, 3-D structural models are needed to accurately model coupling and load paths and the non-beam-like parts of the system obtained directly from the CAD. They are needed for ends, short beams, open sections, transitions, and joints—as it is always a problem to make beam models fit all rotor blade parts. This vision was realized with the introduction of X3D [37]. X3D is a University of Maryland/U.S. Army aeroelastic solver built with 3-D finite elements unified with multibody dynamics. Hinges and bearings are simulated using joints, and flexible parts are simulated using 27-noded hexahedral solid finite elements. Despite proving its viability, its extensive use was limited by high computational time. The recent integration of parallel and scalable solvers in X3D [38] has made it feasible for application to large-scale problems. This has opened the opportunity for studying coaxial models.

A modern coaxial rotor involves a complex hub. The existing rotor models with open access, such as the UMD-UTA coaxial rotor [22], do not capture the complexity of a modern coaxial aircraft. The ones that do capture are usually with restricted access. Hence, there is a need for an open-source 3-D rotor model. For this purpose, Metaltail—a hingeless coaxial rotorcraft—is developed for the United States. DoD's High Performance Computing framework Helios. Unlike the regular edgewise coaxial rotorcraft, it is a tail-sitter proprotor aircraft designed for axial flight. Its hingeless rotor hub is intricate with multiple load paths and better represents the complexity of a modern coaxial aircraft. Along with its development, aeromechanical analysis is performed at low-speed transition flight with lifting line aerodynamics. Due to its highly twisted blades, the nature of predictions obtained for this rotor do not represent a real coaxial rotor, but nevertheless qualitative comparisons are made with the S-97 data published in Refs. [9,10]. Detailed 3-D stresses are presented and examined in the context of capability demonstration.

B. Organization of the Paper

Following this introduction, this paper begins with a detailed description of the 3-D structural model of the coaxial Metaltail rotor. The next section briefly describes the UH-60A-like coaxial rotor. The following section covers the refinements performed on baseline X3D for extending to coaxial rotors. The next section validates the refined solver with test data. The subsequent sections discuss the aeromechanics predictions of the single and coaxial Metaltail rotor models. Predictions of performance, airloads, vibratory hub loads, and 3-D stress distribution are examined. Finally, some conclusions are drawn.

II. Metaltail Coaxial Model

Metaltail is a notional coaxial tail-sitter proprotor aircraft designed by the University of Maryland as a part of the 2018 Vertical Flight Society Student Design Competition [39]. It is an open-source research rotor therefore adopted by the U.S. Army/DoD CREATE^{TM}–AV Helios development team as an example case. Figure 2 shows the computer-aided design (CAD) model of the coaxial rotor. Table 1 lists the important rotor parameters. The model shares certain

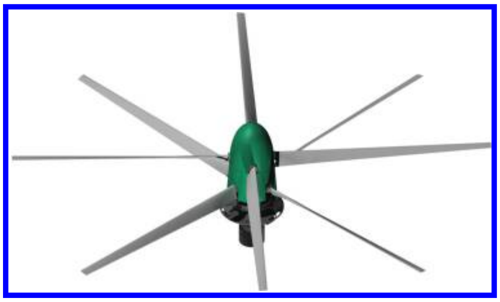

Fig. 2 CAD model of Metaltail coaxial rotor.

Table 1 Properties of Metaltail rotor

Property	Value
Radius, R	1.5 m (4.9 ft)
Number of blades, N_b	4 (each rotor)
Precone	1.5°
Solidity, σ	0.0637 (each rotor)
Rotor separation, z/D	0.07
Rotor speed, Ω	1408 RPM (147 rad/s)
Nominal twist rate,	−56° per span

basic similarities with the S-97 coaxial rotor such as the hingeless hub, four blades on each rotor, and similar inter-rotor spacing. One major deviation from S-97 is its highly twisted blades uncharacteristic of an edgewise rotor. Nevertheless, it is retained as the high twist along with the intricate hub involves all the complications possibly required for modeling a modern coaxial rotor.

A. CAD Model

The first step in the 3-D modeling procedure is to develop the CAD model in CATIA. Figure 3 shows the CAD model of individual parts of the Metaltail blade. It consists of the following parts—the blade, pitch horn, pitch link, inner cuff, outer cuff, thrust bearing, and journal bearing. The connectivity between each of these parts is described using the structural analysis representation below.

B. Structural Analysis Representation (SAR)

The structural analysis representation assigns which parts are to be modeled using 3-D finite elements and which parts are to be simply modeled as joint connections. It then defines the type and geometry of joint connections and assigns joint properties. The present model has five flexible parts: the blade, pitch horn, pitch link, inner cuff, and outer cuff. The bearings, fittings between the flexible parts, and hub connections are modeled as joints. Figure 4 shows the attachment of

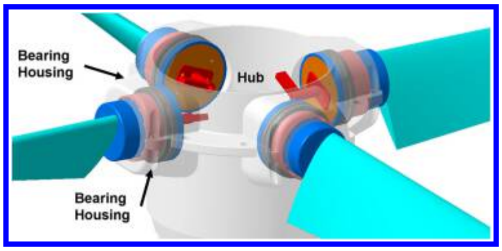

Fig. 4 Attachment of Metaltail rotor blade root to hub through bearing housing.

the blade root to the hub. The blade root is sandwiched by the bearing housing from top and bottom, which connects the thrust and journal bearings to the hub. The pitch horn is assembled at the root of each inner sleeve and connected to the upper swashplate (not shown in Fig. 4) with a pitch link.

The bolts between the inner cuff and the outer cuff, the thrust and journal bearings, and pitch link connections to the pitch horn and hub are modeled as joints. The exposed root of the blade mates into the inner surfaces of the outer cuff, and the inner cuff locks into the open slot of the blade, as shown in Fig. 5b. So, the connections between the blade and both the cuffs are modeled as rigid joints. The outer cuff is connected to the rotor hub through two bearings, as shown in Fig. 5a. The thrust bearing transfers only axial force to the hub. The journal bearing transfers thrust, in- and out-of-plane shears, and the flapping and lead-lag moments. The inner cuff is connected to a pitch horn, which is then connected to a pitch link on the leading-edge side of the blade. The torsion moment is transferred via the inner cuff to the pitch link connection to the hub.

In total, the model has 13 parts, 5 of which are flexible parts and 8 are joints. These are shown in Fig. 6 and listed in Table 2. Figure 7 shows the load flow diagram. Each part has two ID numbers, one is the part number (P#), and another is the type number (F# for flex parts, J# for joint parts). The five flexible parts are meshed using brick finite elements. The eight joint parts are assigned kinematic constraints using Euler angles. Three joints are connected to the hub. The identifier −1 sets zero displacement boundary condition (in the rotating frame). Here, it is the hub. Vertical motion commanded to the joint (P1/J1) provides pitch control for trim solution.

The hub is rigid, so the upper and lower rotors are independent with no dynamic interactions. The analysis is carried out using a single blade in each rotor. There are three connections to the hub for each rotor blade, as seen in Fig. 7. Hence for the coaxial model, there are a total of six connections to the hub, three from each rotor.

C. X3D Structural Analysis Model (SAM)

Once the part types are assigned, the individual flexible parts are meshed in Cubit. Part meshes are independent. The meshes are generated using 27-node isoparametric hexahedral brick elements.

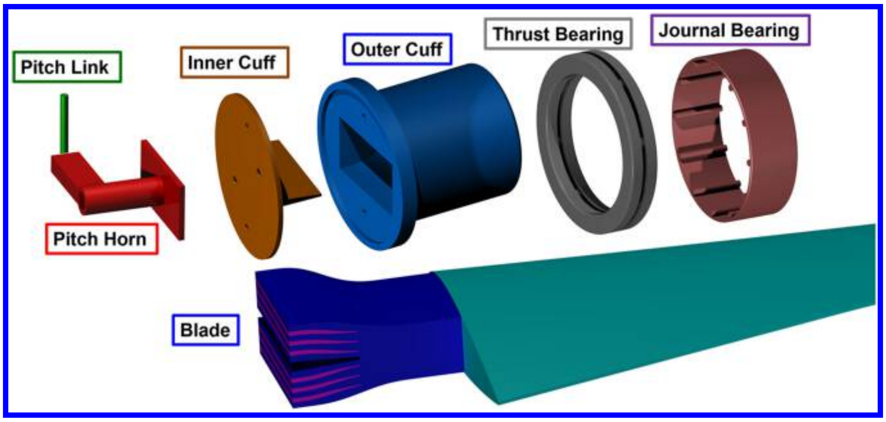

Fig. 3 CAD model of the Metaltail rotor blade showing five flexible components and two bearings.

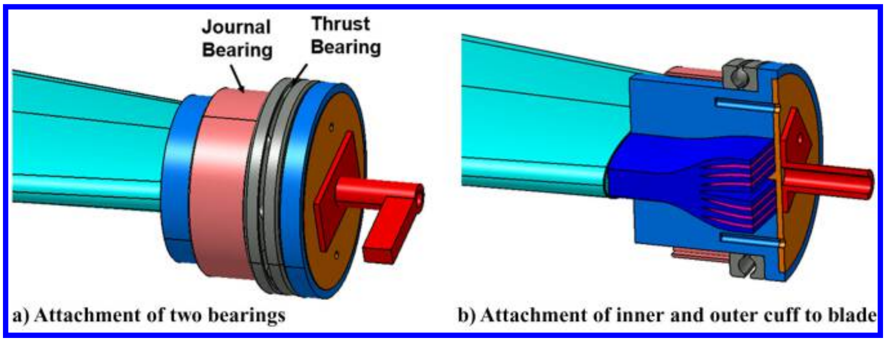

Fig. 5 Cut-away view of blade root showing attachment of a) thrust and journal bearing, and b) inner and outer cuff to blade.

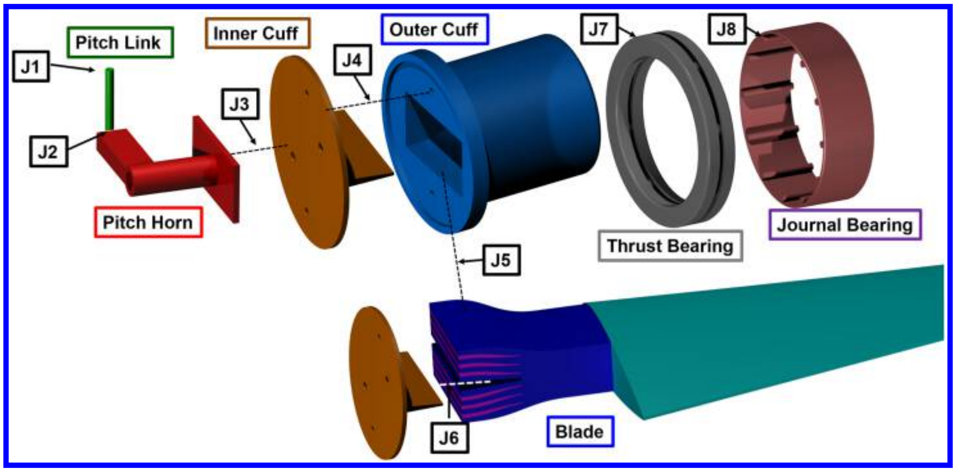

Fig. 6 Joints in the Metaltail model; eight joints J1–J8 modeled for various purposes.

Table 2 List of parts in the Metaltail blade structural model, including connections with −1 indicating a connection to the hub

Part No.	Flexible/Joint No.	Name	Type	Connections
P1	J1	jPlinkHub	Joint	−1, P2
P2	F1	Pitch Link	Flex	P1, P3
P3	J2	jPlinkPhorn	Joint	P2, P4
P4	F2	Pitch Horn	Flex	P3, P5
P5	J3	jPhornIcuff	Joint	P4, P6
P6	F3	Inner Cuff	Flex	P5, P7, P11
P7	J4	jIcuffOcuff	Joint	P6, P8
P8	F4	Outer Cuff	Flex	P7, P10, P12, P13
P9	F5	Blade	Flex	P10, P11
P10	J5	jOcuffBlade	Joint	P8, P9
P11	J6	jIcuffBlade	Joint	P6, P9
P12	J7	jThrustBearing	Joint	−1, P8
P13	J8	jJournalBearing	Joint	−1, P8

A detailed description of meshing rotor blades can be found in Ref. [40]. The meshes and joints are assembled to create the final structural analysis model of the blade, as shown in Fig. 8. It consists of 1316 bricks with a total of 31,735 degrees of freedom. For coaxial configuration, the blades of both rotors are meshed and assembled together, as shown in the Fig. 9. It consists of twice the number of degrees of freedom as the single rotor model.

Each part mesh is assigned three features: blocks (B), sidesets (SS), and nodesets (NS). These are also generated in Cubit. They are used by the solver for important tasks. Blocks assign materials for flexible parts, sidesets identify aerodynamic surface nodes, and nodesets list the finite element nodes to which joints connect.

The meshes and joints are input to the solver through the *SAM.input* file. This file can be made manually or automatically using the Python-based utility samBuilder [40]. The *SAM.input* is a FORTRAN name

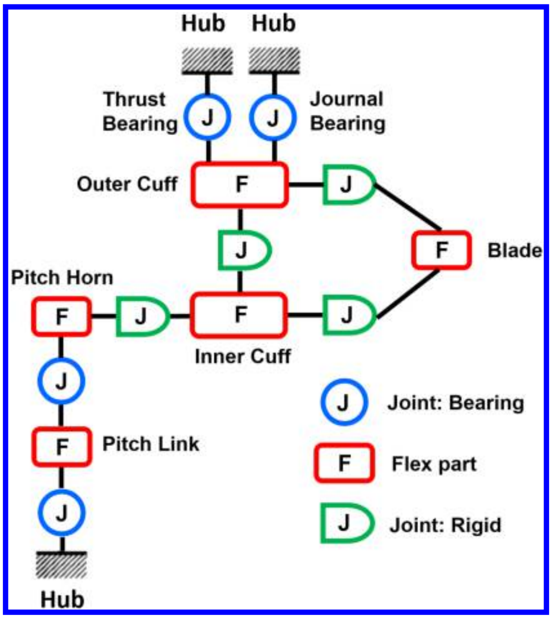

Fig. 7 Load flow diagram for the Metaltail rotor blade structural analysis model.

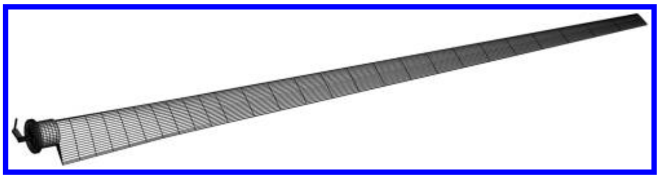

Fig. 8 Assembled structural mesh of the Metaltail blade.

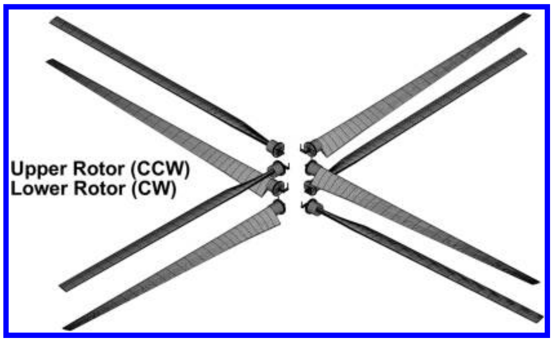

Fig. 9 Assembled structural mesh of coaxial Metaltail.

list consisting of mesh positions and orientations, material properties, joint properties, and joint connections.

D. X3D Aerodynamic Model (AER)

The aerodynamic model of the blade is input through the *AER.-input* file. It is a FORTRAN name list of airfoil names and lifting line properties, similar to any beam-based comprehensive analysis. The Metaltail blade consists of two airfoils: NACA2420 at the root and SC1095 at the tip. The transition between the root airfoil and the tip airfoil occurs at $30\%R$. The blade is highly twisted at a nominal rate of $-56°$ per span. The chord and twist distribution can be found in Ref. [39].

E. X3D System Definition (SDN)

The system model is input through the *SDN.input* file. It is a FORTRAN name list of atmospheric properties, aircraft geometry, number of rotors, rotor–rotor separation distance (z/D), and other top-level parameters. The file is also similar to any beam-based comprehensive analysis.

III. UH-60A-Like Coaxial Model

A notional coaxial configuration using articulated UH-60A-like rotors is developed as it provides the benefit of being a realistic edgewise rotor with moderate twist, thereby useful for qualitative comparison with the aeromechanics predictions of Metaltail and S-97 Raider data. The inter-rotor separation is kept identical to Metaltail ($z/D = 0.07$). This coaxial rotor uses a representative model of an UH-60A rotor blade, which is the exact model studied and validated in Ref. [38]. The internal structure of the blade is an idealization, reverse engineered to reproduce similar fan plot as the real rotor. The external geometry and aerodynamic description including airfoil decks are nearly exact and follow the Army-NASA Database. A pitch bearing coincident with the flap and lag hinge is co-located at $4.66\%R$. The bearing also includes a linear lag damper. The control inputs are provided through joint commands at the pitch bearing. Overall, each blade of the coaxial rotor is connected to the hub through a single joint. Figure 10 shows the 3-D model of the blade. There are 592 hexahedral bricks with a total of 17,523 degrees of

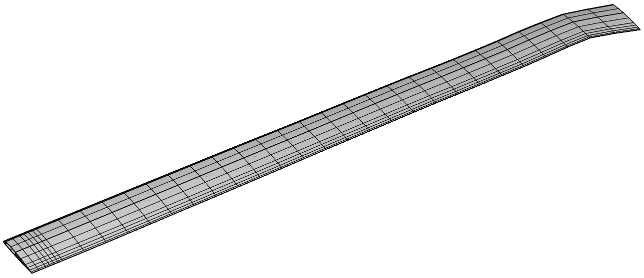

Fig. 10 Three-dimensional brick mesh of an UH-60A-like articulated rotor; aerodynamic description is exact (based on Ames database); only the trailing edge tab is ignored; the flap, lag, and torsion bearing are at $4.66\%R$.

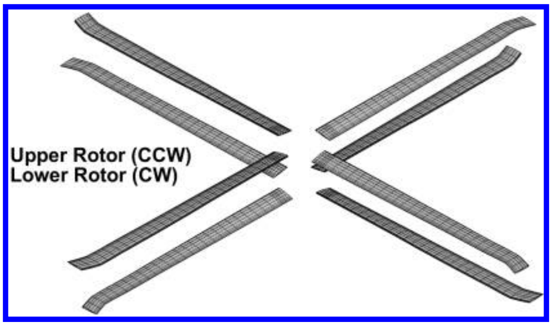

Fig. 11 Assembled structural mesh of UH-60A-like coaxial rotor configuration.

freedom. Figure 11 shows the assembled structural mesh for the coaxial UH-60A model. It consists of twice the number of degrees of freedom as the single rotor model.

IV. Coaxial X3D Solver

X3D is a University of Maryland/U.S. Army 3-D aeroelastic solver [37]. Recently, a scalable and parallel harmonic balance method was integrated into X3D [38]. This new version is executed on a hybrid distributed and shared memory computer architecture. It was validated with UH-60A rotor flight test data [38] and the NASA Tilt Rotor Aeroacoustic Model (TRAM) proprotor DNW wind tunnel data [41]. The present version of X3D is extended for modeling coaxial rotors through the following refinements.

A. Structural Dynamics

The structural dynamics module of X3D was modified to allow modeling of an arbitrary number of rotors spinning in counterclockwise (CCW) or clockwise (CW) directions. X3D carries out the nominal analysis in a right-handed CCW frame. To model CW rotation, the calculations are performed as a CCW rotor, with the conditions, motions, and loads changing signs appropriately. For example, the wake analysis is in the fixed frame, so blade motions into the wake and inflow out of the wake are adjusted appropriately. The hub forces and moments for CW rotation can be obtained from the nominal analysis by changing the signs according to Eq. (2), where F_X^{CCW}, F_Y^{CCW}, F_Z^{CCW}, M_X^{CCW}, M_Y^{CCW}, are M_Z^{CCW} are the calculated values with CCW rotation.

$$\begin{aligned} &F_X^{\mathrm{CW}} = F_X^{\mathrm{CCW}}; \quad F_Y^{\mathrm{CW}} = -F_Y^{\mathrm{CCW}}; \quad F_Z^{\mathrm{CW}} = F_Z^{\mathrm{CCW}}; \\ &M_X^{\mathrm{CW}} = -M_X^{\mathrm{CCW}}; \quad M_Y^{\mathrm{CW}} = M_Y^{\mathrm{CCW}}; \quad M_Z^{\mathrm{CW}} = -M_Z^{\mathrm{CCW}} \end{aligned} \tag{2}$$

B. Aerodynamics

The aerodynamics of the coaxial rotors were modeled using quasi-steady lifting line theory coupled with time-accurate free wake. The Maryland Free Wake (MFW) is a product of several research efforts over the years by Bagai and Leishman [28,42,43], Bhagwat and Leishman [44–47], and Ananthan and Leishman [48]. The original MFW model was updated to a new version by Shastry and Datta [49] that can analyze variable and transient RPM (including stopped rotor) on multiple rotors even though that feature is not used in the present work. The original model has the ability to study coaxial rotors as showcased in Refs. [28,29]; however, these models were developed in the azimuth domain, assuming a single fundamental rotor speed. The new model was developed using a time-domain-based formulation. The governing equations are still solved using the Predictor-Corrector Second-order Backward (PC2B) scheme by Bhagwat and Leishman [45], and details of implementation are found in Ref. [49]. This new wake model is used to capture the inter-rotor interactions in a coaxial rotor.

C. Trim

The analysis provides multiple options for coaxial trim. The upper and lower rotor collectives provide total thrust and torque balance.

The cyclics can be solved with two options. In the first option, the lateral ($\theta_{1c}^U, \theta_{1c}^L$) and longitudinal ($\theta_{1s}^U, \theta_{1s}^L$) cyclics can be solved for specified roll and pitch moments on each rotor. This option is useful for fundamental understanding and research and is used in this work. In the second option, the lateral cyclic is kept same for both upper and lower rotors ($\theta_{1c}^U = \theta_{1c}^L = \theta_{1c}$), and this value along with the two longitudinal ($\theta_{1s}^U, \theta_{1s}^L$) cyclics is solved for a specified lift offset and total zero roll and pitch moments. The second option is similar to the actual aircraft trim.

V. Validation of Hover Aerodynamics

The wake is first validated with coaxial hover performance data from the U.S. Army model test [4]. The test was conducted on a rigid coaxial rotor, with each rotor consisting of three blades. Table 3 shows the rotor properties. The X3D model is also rigid with a nominal rotor separation of 7% diameter ($z/D = 0.07$). The blades are untwisted and rectangular with NACA 0012 airfoil. The tip Mach number was very low (0.25). The tip Reynolds number (325,000) was low enough that Reynolds number corrections are needed. The near wake is prescribed, and the far wake is free consisting of a rolled-up single tip vortex from each blade.

Figure 12 shows the upper and lower rotor performance in hover in the coaxial state. The collective was swept with net zero torque trim condition at each collective. For the same torque, the lower rotor produces less thrust as it is in climb due to the wake from the upper rotor. The effects of rotor–rotor influence were studied by varying the rotor separation distance. Figure 13 shows the predictions and measurement data of thrust coefficient as a function of rotor separation distance for two total thrust conditions: low thrust ($C_T = 0.007$) and high thrust ($C_T = 0.014$). The torque coefficient variation is shown in Fig. 14. Figure 15 shows the free wake geometry of coaxial wake in hover for separation distance $z/D = 0.07$ and $z/D = 1.5$. Regardless of the total thrust (low or high thrust), with increasing separation, the lower rotor produces a lower thrust until the wake of the upper rotor is fully developed. Thereafter, the thrust sharing is constant—around 55% for the upper and 45% for the lower rotor. As the rotors get closer, the upper rotor thrust decreases due to the influence of the lower rotor, as seen in Fig. 13. Overall, the X3D analysis shows good agreement with the test data.

Table 3 Properties of the rigid rotor from U.S. Army model test

Property	Value
Radius	0.66 m (2.17 ft)
Number of blades	3
Chord	0.0647 m (0.19 ft)
Nominal rotor separation, *z/D*	0.07
Airfoil	NACA 0012
Rotor speed	1200 RPM (125.66 rad/s)

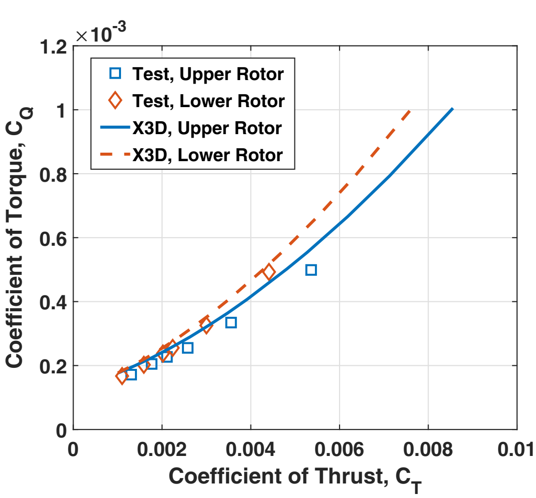

Fig. 12 Upper and lower rotor performance of coaxial rotor in hover; predictions compared with measurements.

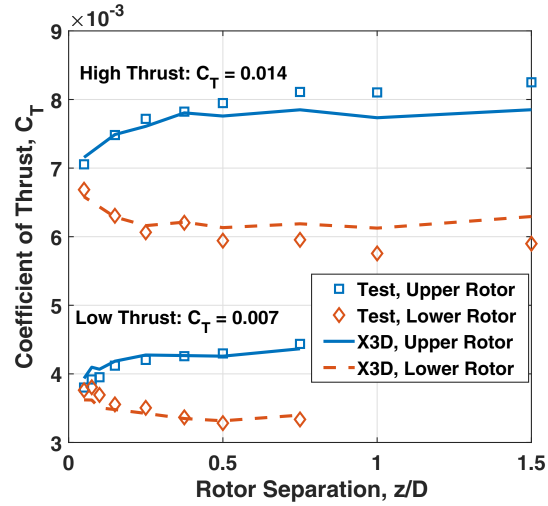

Fig. 13 Upper and lower rotor thrust coefficient in hover vs various rotor separation distances for two thrust conditions; predictions compared with measurements.

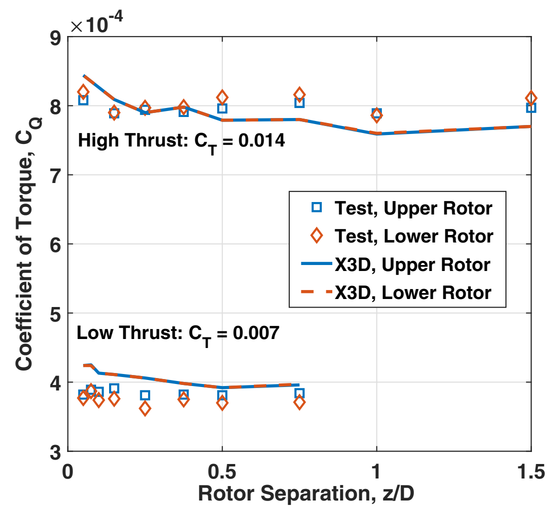

Fig. 14 Upper and lower rotor torque coefficients in hover vs various rotor separation distances for two thrust conditions; predictions compared with measurements.

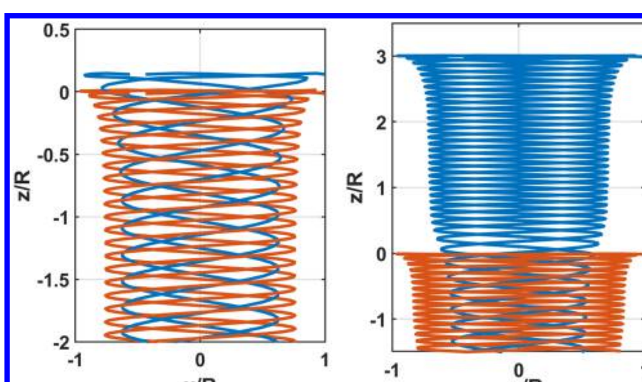

a) z/D = 0.07 b) z/D = 1.5

Fig. 15 Free wake geometry of coaxial wake in hover for two separation distances: a) $z/D = 0.07$; b) $z/D = 1.5$.

VI. Verification of Forward Flight Aerodynamics

In the absence of public domain property data on the X2 or S-97 helicopters for thorough X3D validation, the notional coaxial UH-60A-like rotor model is used. This validation is more of a sanity check that verifies the working of all the refinements made in the X3D solver. The verification is performed on the limiting case of infinite separation between the rotors. At this separation, there are no rotor–rotor interactions, and both upper and lower rotors are expected to behave as isolated single-rotor helicopters. Predictions of normal force are compared with the flight-test data from UH-60A Airloads Program transition flight C8513. The conditions are $\mu = 0.15$, $\alpha = -3.75°$, and $C_T/\sigma = 0.076$.

The free wake model utilizes a fully rolled-up single-tip vortex model with no near wake. Figure 16 shows the measured and predicted normal forces at different radial stations along the azimuth. Figure 17 shows the corresponding harmonics distribution. The blade lift near tip has higher harmonic contributions (3,4 /rev), owing to the wake roll up near advancing and retreating sides of blades. This level of accuracy is consistent with the state-of-the-art lifting-line free wake models.

VII. Single Main Rotor Metaltail

A. Test Conditions

The single rotor Metaltail was studied first to better understand the effects of rotor–rotor interactions in a coaxial system later. Predictions are obtained for edgewise flight at advance ratio $\mu = 0.1$, forward shaft tilt $\alpha = -2°$, and $C_T/\sigma = 0.08$. The trim targets are thrust and zero hub moments. The low speed allows for verifying the predictions qualitatively with the TRAM test data [41,50]. The results are generated with two aerodynamic inflow models: linear inflow and free wake and are compared against each other.

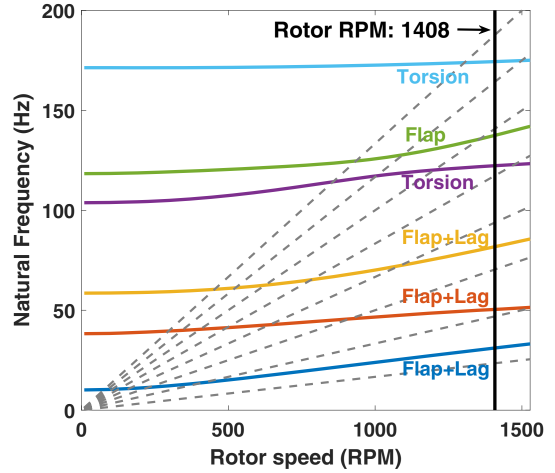

Fig. 18 **Rotating frequencies for the Metaltail structural analysis model.**

B. Rotor Frequencies

The rotor frequencies are shown in Fig. 18. At the nominal rotational speed of 1408 RPM, the frequencies clear all the rotor harmonics. The flap and lag modes are coupled due to high twist. The first flap-lag frequency is 1.3 /rev, and the first torsion is 5.22 /rev. The high first flap frequency is not unusual for modern coaxial rotors. The first six natural frequencies are provided at the operating rotor speed in Table 4.

C. Airloads

Figures 19 and 20 show the normal force predictions in the time and frequency domain at two radial stations: 72%R and 90%R. The

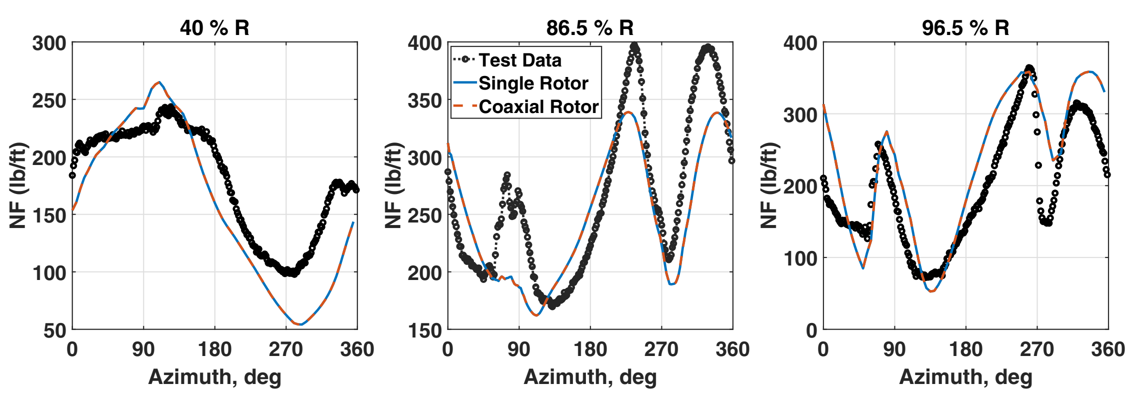

Fig. 16 **Normal force distribution along azimuth at different radial stations; predictions compared with measured flight test data; verifies coaxial airloads at infinite separation.**

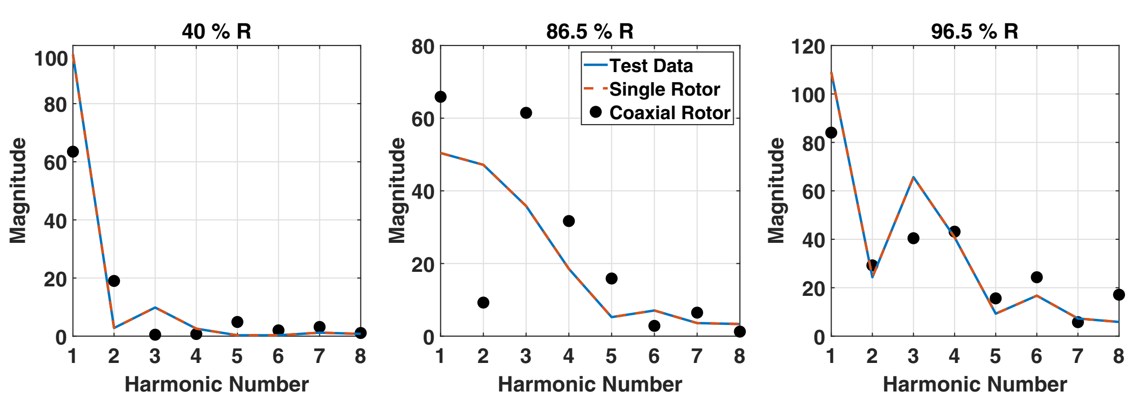

Fig. 17 **Harmonics distribution of normal force along azimuth at different radial stations; predictions compared with measured flight test data.**

Table 4 First six blade frequencies in vacuum at 1408 RPM

Mode	Frequency (/rev)
First flap/lag	1.33
Second flap/lag	2.15
Third flap/lag	3.48
First torsion	5.22
Fourth flap	5.85
Second torsion	7.43

linear inflow model can only capture the gross 1/rev characteristics of the airloads. The free wake model predicts higher harmonics with the characteristics of vortex loadings in the first and fourth quadrant near the tip. The lift near tip has a significant 4/rev, as shown in Fig. 20b.

VIII. Coaxial Rotor Metaltail

A. Test Conditions

The predictions for coaxial Metaltail shown in this paper are obtained at exactly the same conditions as the single rotor. The only difference is that an additional roll moment target of 10%R lift offset is considered. The choice of low-speed flight ($\mu = 0.1$) allows for qualitative comparison with the S-97 Raider loads published recently in Refs. [9–11]. Some of the predictions for performance and vibratory loads are obtained for a range of advance ratios. Only the free wake model is used with a fully rolled-up single tip trailer.

The periodic rotor solution was obtained using the modified harmonic balance (MHB) algorithm [38] with the rotor solution consisting of eight harmonics and executed on a hybrid distributed—shared memory architecture with 90 processors. The 6-degree-of-freedom trim solution for a coaxial rotor requires around 50 min of wall clock time. The free wake model is parallelized with shared memory OpenMP processors, with the number of processors equal to the number of tip trailers (eight in our case). The free wake computations for each trim iteration require 1 min wall clock time for 10 wake turns and 20 revolutions in time with 7.5° time step.

B. Performance

Predictions of the rotor lift-to-equivalent drag ratio (L/D_e) with the advance ratio for several lift offsets are shown in Fig. 21. The rotor L/D_e is defined by

$$L/D_e = \frac{C_T}{(|C_Q^U| + |C_Q^L|)/\mu + C_X} \tag{3}$$

where $C_T = C_T^U + C_T^L$ is the total thrust, and $C_X = C_X^U + C_X^L$ is the total propulsive force. The only change from single rotor is the sum of absolute torques $|C_Q^U| + |C_Q^L|$. The Metaltail rotor has a very low L/D_e, typical of a proprotor in helicopter mode. This is due to the highly twisted blades. Regardless of the lift offset, the rotor L/D_e increases with the advance ratio until around $\mu = 0.3$. An increase in lift offset helps to increase the cruise performance of the rotor only after a certain advance ratio, which is around $\mu = 0.2$. However, a

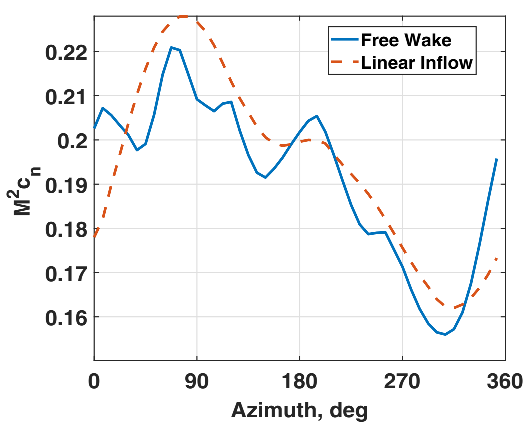

a) Normal force at 72 % radial location

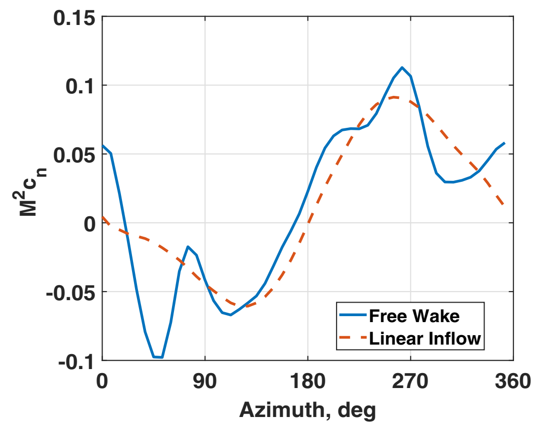

b) Normal force at 90 % radial location

Fig. 19 Predictions of normal force with linear inflow and free wake models at $\mu = 0.1$, $C_T/\sigma = 0.08$: a) 72%R; b) 90%R.

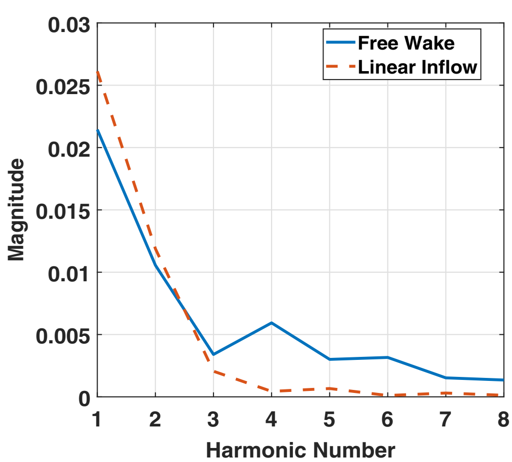

a) Harmonics distribution at 72 % radial location

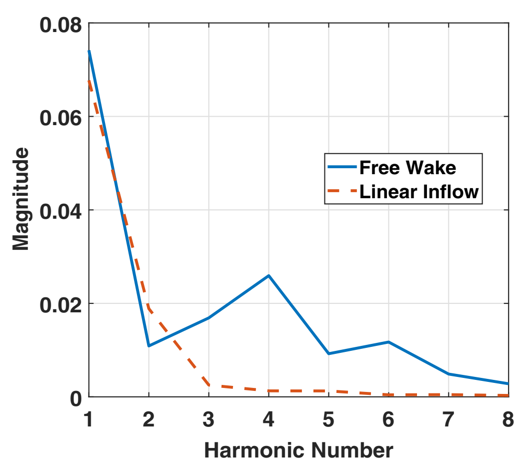

b) Harmonics distribution at 90 % radial location

Fig. 20 Predictions of normal force harmonics with linear inflow and free wake at $\mu = 0.1$, $C_T/\sigma = 0.08$: a) 72%R; b) 90%R.

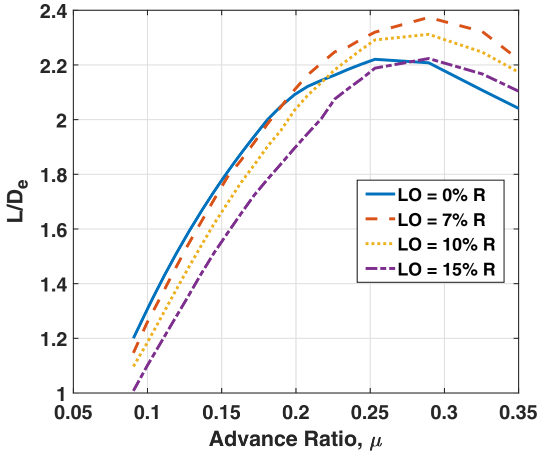

Fig. 21 Coaxial rotor lift-to-equivalent drag ratio vs advance ratio for multiple lift offsets.

very high lift offset ($\geq 10\%R$) does not help much with the performance, and the maximum L/D_e occurs at $LO = 7\%R$.

Figure 22 shows the control angles for both upper and lower rotors for two lift offset cases. The longitudinal cyclic θ_{1s} produces the lift offset because of the high flap frequency. The collectives more or less follow the power curve trend. The lower rotor has a higher trim collective than that of the upper rotor. This is because the lower rotor operates in the wake of the upper rotor and needs a higher collective to produce the same torque.

C. Airloads

Figures 23 and 24 show the normal force predictions in the time and frequency domain at $72\%R$ and $90\%R$, for upper and lower rotors of a coaxial rotor operating with zero lift offset. Note that the azimuth axes in Fig. 23 correspond to the local azimuth of each rotor. The lower rotor has greater contribution from higher frequencies – 3,4,5 / revs. This is attributed to the upper rotor wake impinging on the lower rotor. At low speed, this interaction is significant and can be observed as a magnified impulse in the first quadrant of the lower rotor. This was not visible on the single rotor Metaltail. Figure 25 shows the free wake geometry for the coaxial Metaltail in forward flight. It can be visually seen that the wake at transition flight speed involves noticeable interferences of upper rotor wake on the rear part of lower rotor.

Figures 26 and 27 show the airloads but now with $LO = 10\%R$. With lift offset, as expected, the blade lift increases near the advancing side and decreases near the retreating side. The authors of Ref. [9] discusses the low-speed forward flight analysis of S-97 Raider using CFD/CA analysis. It is mentioned that the upper and lower rotor interactions result in a dominant 3/rev contribution in the lift of lower rotor blade at its tip. However, this dominant 3/rev is not observed for coaxial Metaltail; a dominant 4/rev is seen instead. This dissimilarity was investigated in detail in Ref. [51] and is mentioned here for completeness.

It is not straightforward to investigate the wake effects on a coaxial proprotor. A typical wake field of a proprotor blade involves multiple

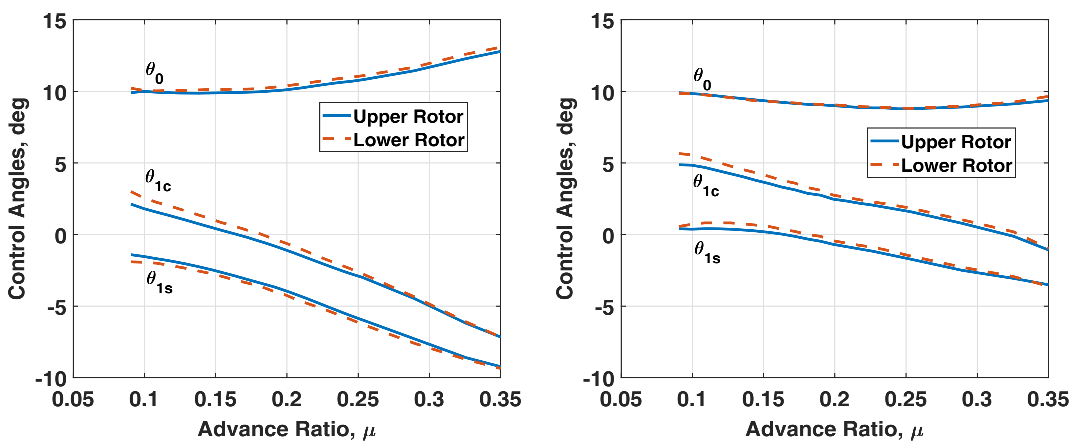

a) LO = 0% R

b) L0 = 10% R

Fig. 22 Coaxial control angles (θ_0,θ_{1c},θ_{1s}) for upper and lower rotor with a) $LO = 0\%R$ and b) $LO = 10\%R$.

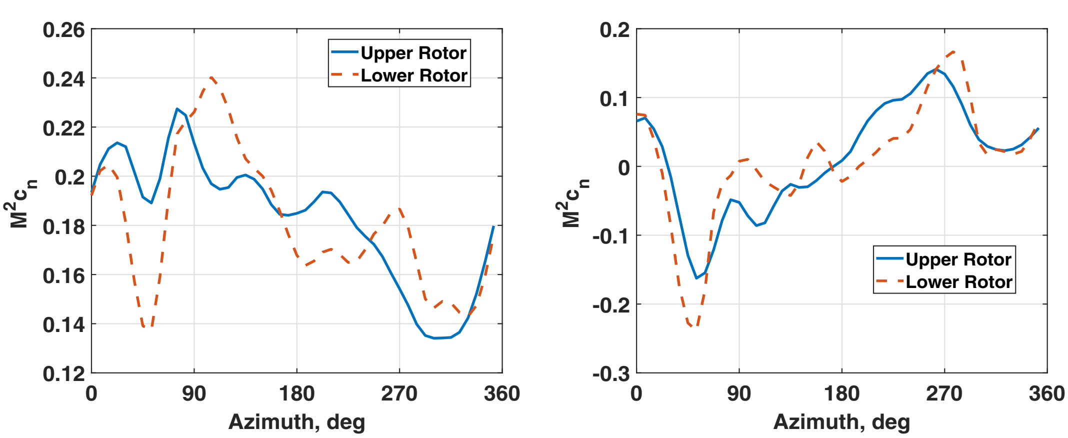

a) Normal force at 72 % radial location

b) Normal force at 90 % radial location

Fig. 23 Predictions of normal force for coaxial rotor with zero lift offset; a) $72\%R$; b) $90\%R$.

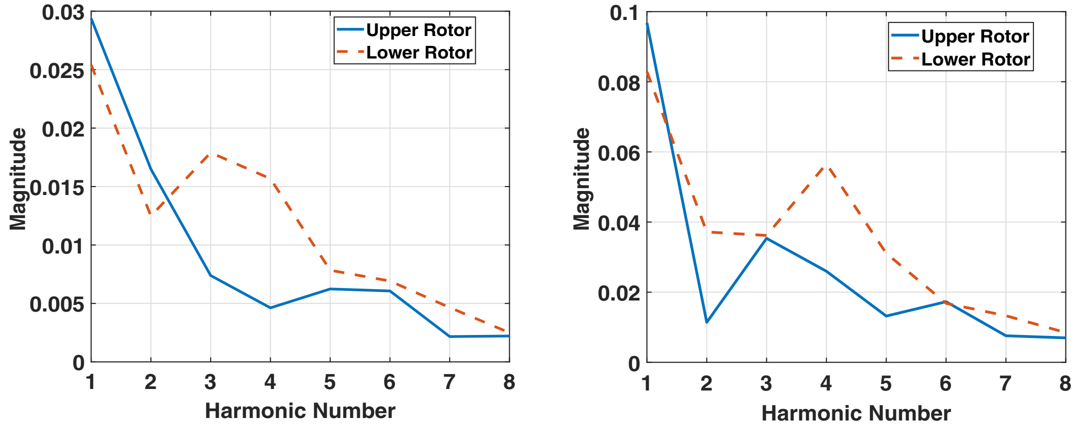

a) Harmonics distribution at 72 % radial location b) Harmonics distribution at 90 % radial location

Fig. 24 Predictions of normal force harmonics for coaxial rotor with zero lift offset; a) 72% R**; b) 90%** R**.**

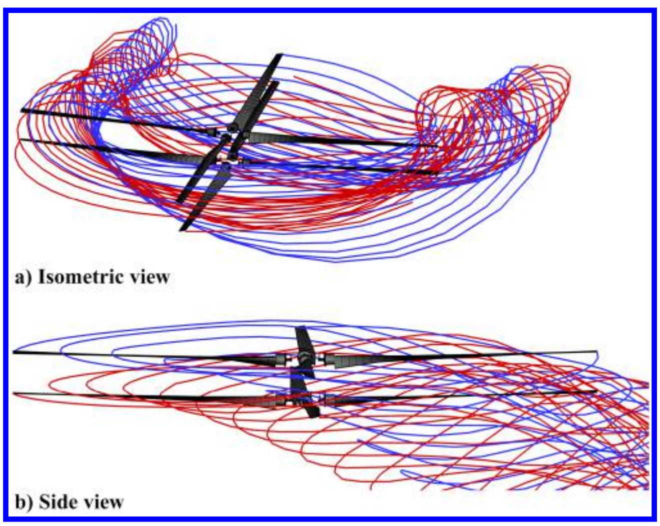

Fig. 25 Free wake geometry for coaxial Metaltail at low-speed flight ($\mu = 0.1$**) in a) isometric and b) side view.**

tip vortices that roll-up into a super vortex. This is different from a typical helicopter rotor, where the full-span trailed wake is rolled up into a single-tip vortex. This is due to the high twist of the proprotor blades, which causes a negative lift near the tip. The proprotor wake roll-up of single rotor Metaltail showed a 4/rev contribution in the blade lift near the tip (Fig. 20). In the coaxial Metaltail, this effect is amplified from both rotors. The high twist in Metaltail is the probable cause of deviation from the S-97 trends. To investigate, the coaxial configuration of the UH-60A-like rotor was used. It is likely to have a twist similar to S-97. Because UH-60A is an articulated rotor, the coaxial version was analyzed with zero lift offset. Figure 28 shows the airloads at the blade tip for the coaxial UH-60A-like configuration. In this case, a dominant 3/rev contribution is indeed observed in the lower rotor, which is similar to the behavior reported for S-97 Raider in Ref. [9]. Thus, twist indeed seems to be the source of deviation.

Figure 29 shows the spanwise distribution of 3/rev and 4/rev normal force harmonics for Metaltail and UH-60A coaxial rotors with $LO = 0\%R$. The airloads are tip concentrated in both cases. For Metaltail, the 4/rev contributions are higher than that of 3/rev, and the contributions of upper and lower rotor are of comparable magnitude with the lower rotor slightly greater. For the UH-60A coaxial rotor, the 3/rev contributions are significantly higher than 4/rev, and the lower rotor shows higher contributions over upper rotor. The nature of the spanwise distribution of airloads shown in Fig. 29b resembles that of the S-97 rotor mentioned in Ref. [11].

D. Hub Loads

Figures 30 and 31 show the predicted upper and lower rotor hub loads with zero and 10%R lift offset, respectively, at $\mu = 0.1$. F_X, F_Y, and F_Z correspond to the longitudinal, lateral, and vertical hub forces, respectively. M_X, M_Y, and M_Z correspond to the rolling, pitching, and yawing hub moments, respectively. The hub loads of both rotors

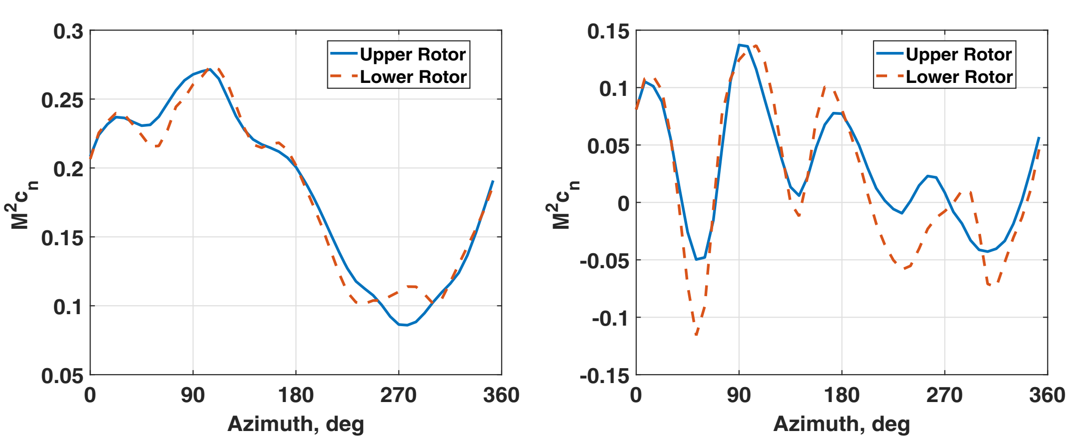

a) Normal force at 72 % radial location b) Normal force at 90 % radial location

Fig. 26 Predictions of normal force for coaxial rotor with 10% R **lift offset: a) 72%** R**; b) 90%** R**.**

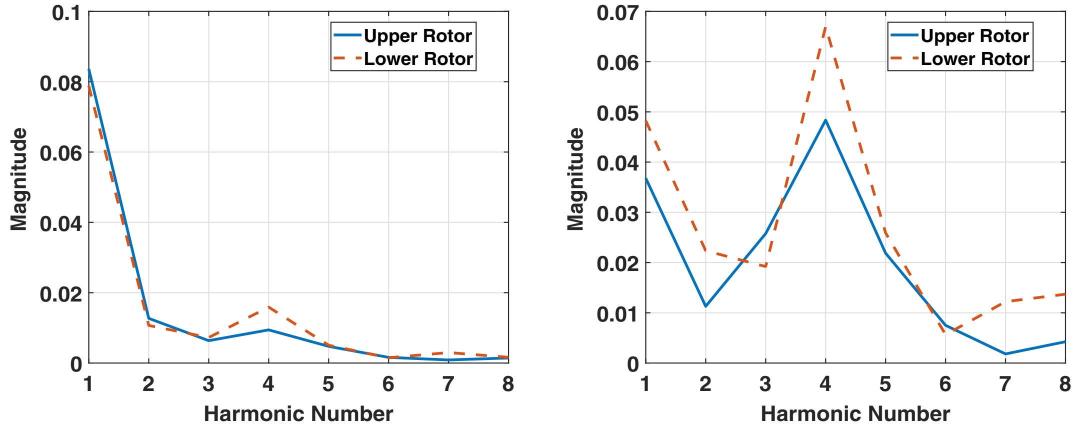

a) Harmonics distribution at 72 % radial location

b) Harmonics distribution at 90 % radial location

Fig. 27 Predictions of normal force harmonics for coaxial rotor with 10% *R* lift offset: a) 72% *R*; b) 90% *R*.

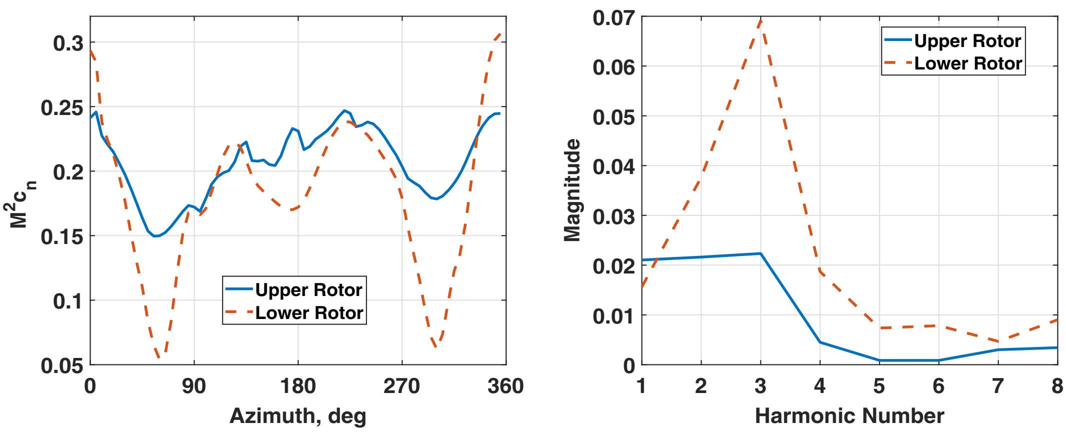

a) Normal force

b) Harmonics distribution

Fig. 28 Predictions of airloads for UH-60A coaxial rotor at 90% *R*: a) normal force; b) normal force harmonics.

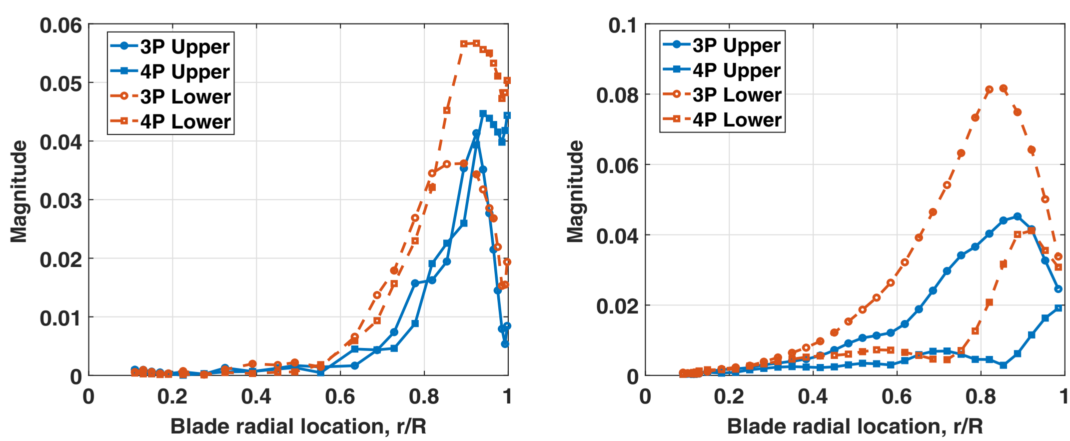

a) Metaltail

b) UH-60A coaxial rotor

Fig. 29 Spanwise distribution of normal force harmonics (3P, 4P) for a) Metaltail and b) UH-60A coaxial rotor.

are dominated by 4/rev contributions because there are 4 blades in each rotor. The total coaxial rotor hub loads are not shown; however, they are obtained as a sum of upper and lower rotors. The upper and lower rotors' contribution cancel each other in the time domain for lateral shear (F_Y), rolling moment (M_X), and torque (M_Z). However, the contributions from each rotor add up for two forces (F_X, F_Z) and pitching moment (M_Y). The time-averaged pitching moment for each rotor is zero; hence, when added, the total contribution is zero. A nonzero lift offset will produce a nonzero time-averaged roll moment contribution for upper and lower rotors (Fig. 31). The total contribution when summed is zero.

Main rotor vibration for a four-bladed rotor is typically characterized by the 4/rev vibratory harmonics. The 4/rev vibratory harmonics of the upper and lower rotors are obtained by harmonic analysis of the hub loads shown earlier. The 4/rev vibratory harmonics for the total coaxial rotor are obtained from the harmonic analysis of total hub loads. Figure 32 shows the predicted 4/rev vibratory harmonics of roll (M_X), pitch (M_Y), resultant moment

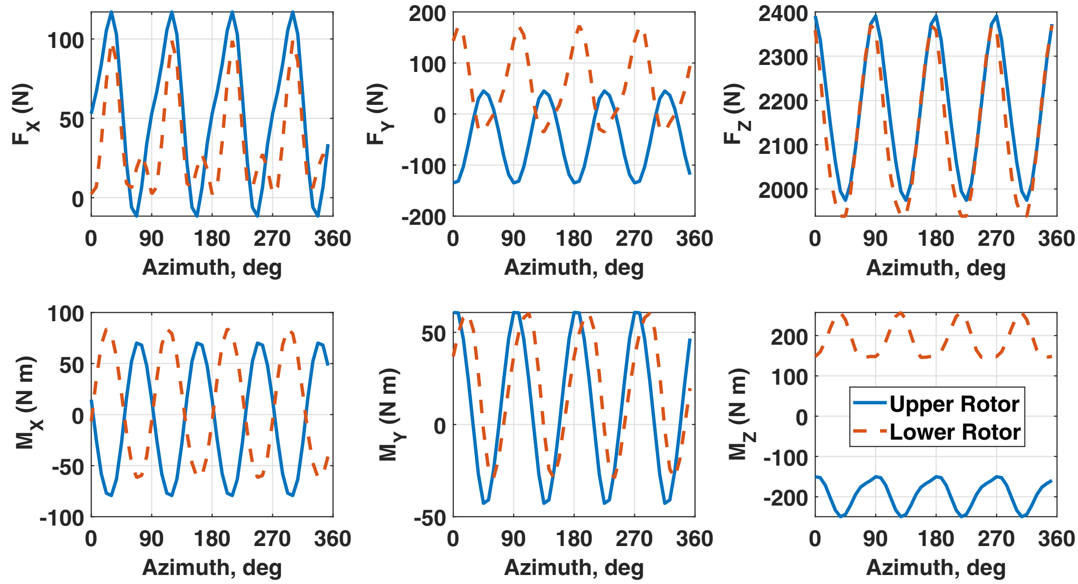

Fig. 30 Vibratory hub forces and moments for Metaltail at $\mu = 0.1$ with zero lift offset.

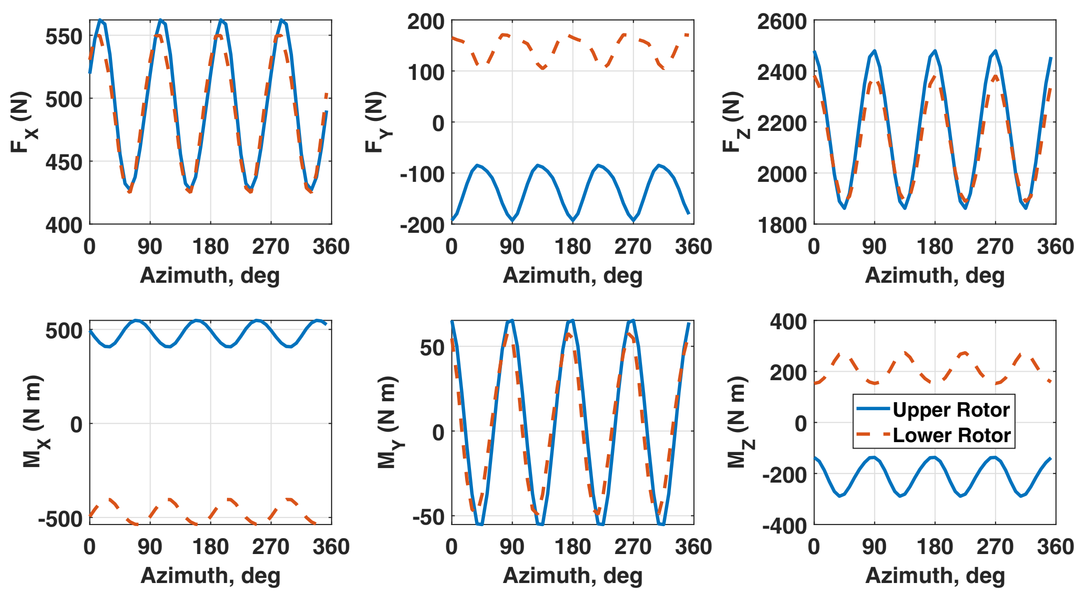

Fig. 31 Vibratory hub forces and moments for Metaltail at $\mu = 0.1$ with 10% R lift offset.

$\left(\sqrt{M_X^2 + M_Y^2}\right)$, and vertical force ($F_Z$) for upper, lower, and total rotor as a function of advance ratio with zero lift offset. As expected, the 4/rev harmonics of hub roll moment for upper and lower rotors cancel each other (Fig. 32a), while the hub pitch moments add up (Fig. 32b). The 4/rev vibratory harmonics of the resultant hub moment $\left(\sqrt{M_X^2 + M_Y^2}\right)$ for the total rotor then takes the form of hub pitch moment (Fig. 32c). The 4/rev vibratory harmonics of F_Z for upper and lower rotors sum up to yield the total contribution (Fig. 32d). The maximum vibration for hub moments was observed at the transition speed ($\mu = 0.1 - 0.15$). The data published in Ref. [9] showed that the maximum vibratory hub moments occur at transition speeds for the S-97 rotor but do not report an exact range of speeds. The 4/rev hub vertical force decreased with increasing advance ratio. There is no consistent trend observed between the contributions of upper rotor and lower rotor to the total 4/rev vibratory harmonics. This is because the upper and lower rotors of Metaltail show similar magnitude of harmonic content in airloads distribution. Similar observations are obtained with 4/rev vibratory hub loads for $LO = 10\%R$, as shown in Fig. 33. For the UH-60A coaxial rotor, it was found that the lower rotor has much higher contributions to 4/rev vibratory harmonics at low speeds than the upper rotor. This was studied and documented in Ref. [51].

E. Inter-Rotor Phase Offset

Inter-rotor phase ϕ represents the angle between the blades of upper and lower rotors in their initial configuration. Figure 34 shows the coaxial rotor arrangement for $\phi = 0°$ and 45°. The rotor phasing changes the magnitude of 4/rev vibratory hub loads. It selectively cancels or sums the vibratory hub loads. At $\phi = 0°$, the roll moments cancel and pitch moments add up for upper and lower rotors. However, at $\phi = 45°$, the roll moments add up and pitch moments cancel for upper and lower rotors. At intermediate angles, the total moments are combination of upper and lower rotors.

Figure 35 shows the total coaxial rotor 4/rev vibratory harmonics of roll (M_X), pitch (M_Y), resultant moment $\left(\sqrt{M_X^2 + M_Y^2}\right)$, and vertical force ($F_Z$) for different phase offsets as a function of advance ratio with $L0 = 10\%R$. The predictions take into account the effects

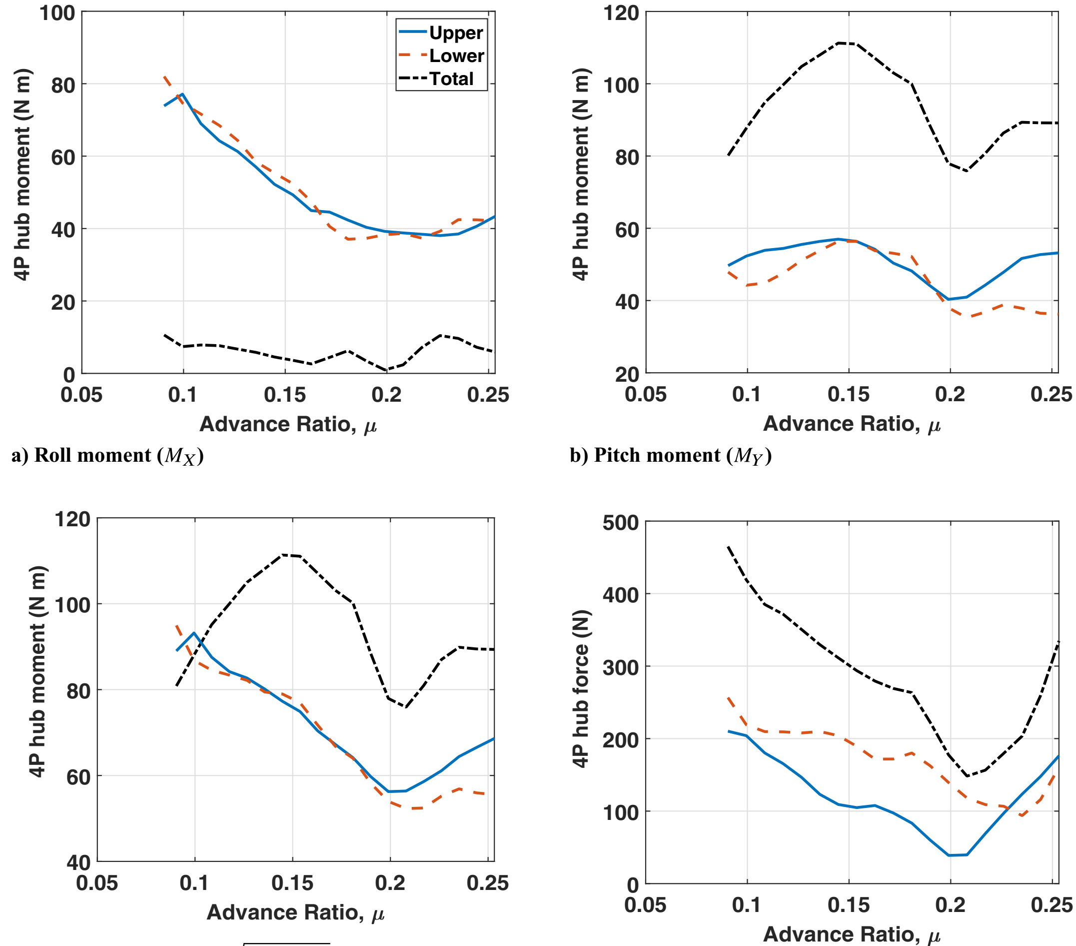

a) Roll moment (M_X)

b) Pitch moment (M_Y)

c) Resultant moment ($\sqrt{M_X^2 + M_Y^2}$)

d) Vertical force (F_Z)

Fig. 32 Predicted 4/rev vibratory harmonics of hub loads for Metaltail at low-speed flight with $LO = 0\%R$.

of wake interactions. Based on the total hub moments, $\phi = 0°$ provides the lowest 4P vibratory harmonics. However, for the hub force (F_z), $\phi = 45°$ provides the lowest 4P vibratory harmonics. An overall choice of phase offset can be made by comparing the magnitudes of the hub loads studied. In this case, there is a larger drop in the magnitude of hub force (F_z) for $\phi = 45°$ from $\phi = 0°$ when compared with the drop in magnitude of hub moments $\left(\sqrt{M_X^2 + M_Y^2}\right)$ for $\phi = 0°$ from $\phi = 45°$. Hence, the choice of $\phi = 45°$ seems more logical for reducing rotor vibration.

F. Three-Dimensional Stress Distribution

The primary benefit to full 3-D FEA-based structural modeling is the ability to predict stresses and strains throughout the rotor, including the hub components. The plots shown here provide only a sample of the results generated, but a wealth of data are available for in-depth analysis. Figures 36 and 37 show the axial/bending stresses (σ_{11}) for Metaltail with $LO = 0\%R$ and $10\%R$, respectively. The highest stresses occur near the advancing and retreating sides of both rotors. For $LO = 0\%R$, the negative blade lift on the advancing side causes downward bending, and higher positive lift on the retreating side causes upward bending. Hence the blades of both rotors are closest at $\psi = 90°$ and farthest at $\psi = 270°$. With $LO = 10\%R$, the advancing side produces more positive lift compared to retreating side to produce the individual rotor roll moment. Hence the blades of both rotors are closest at $\psi = 270°$ and farthest at $\psi = 90°$.

Figures 38 and 39 show the internal axial/bending stresses within the blade for $LO = 10\%R$ at $\psi = 90°$ and $270°$, respectively. Examination of cross section reveals that the blade spar takes most of the bending stress, but there appears to some stress carried by the leading-edge weight. Note that the blade is made up of a solid D'spar. The stress distribution along the span follows the blade bending. This is determined by two factors: the normal lift force and the centrifugal force. The precone in the blade results in a downward bending even without aerodynamics. Consider the case with $LO = 10\%R$ at $\psi = 90°$ shown in Fig. 38. The positive lift at the tip causes a upward bending of the blade. This is seen as compression on top and extension on bottom surface. This effect is more visible near the root. Moving outboard, the moment due to lift force decreases and the centrifugal force bends the blade down. This is seen as extension on top and compression on bottom surface. Similar observations can be obtained with other cases.

Figure 40 shows the same axial stresses at blade root connections to hub at different azimuths for $LO = 10\%R$. The lower rotor has a slightly higher stress than the upper rotor for this case. The blade root connection to the outer cuff shows high stress concentration, as stress in the blade spar is transferred. Otherwise, the outer cuff is under fairly low stress. The inner cuff shows some localized stress concentrations near the outer edge.

IX. Conclusions

This paper presented the first application of high-fidelity 3-D solid FEA structural dynamics to perform aeromechanical analysis of a coaxial rotor. The X3D solver was extended to model coaxial rotors. Two coaxial model test cases were developed. One is the Metaltail, a hingeless coaxial proprotor aircraft, and the other is a coaxial rotor obtained using articulated UH-60A-like rotors. Metaltail was the primary focus of this work. Predictions of performance, airloads, and vibratory hub loads generated with free wake lifting

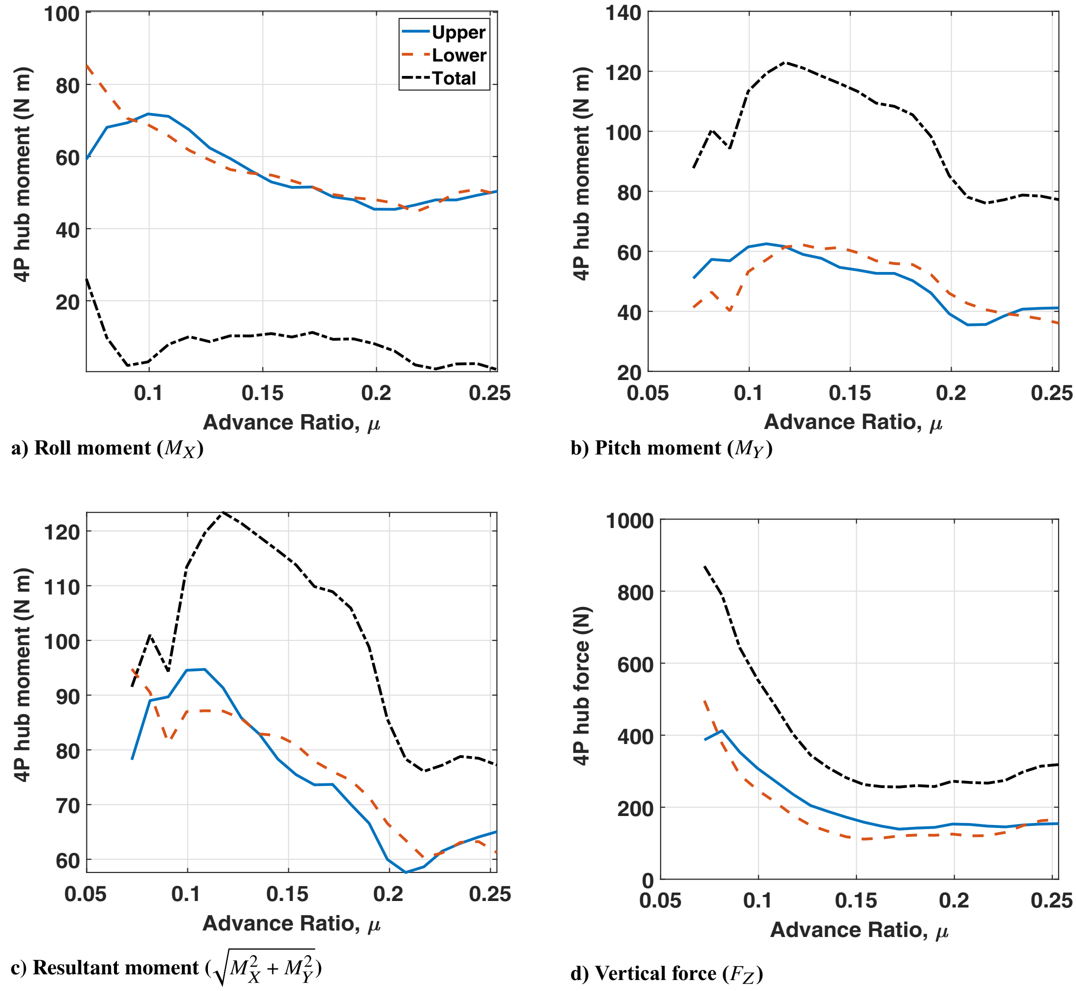

a) Roll moment (M_X)

b) Pitch moment (M_Y)

c) Resultant moment ($\sqrt{M_X^2 + M_Y^2}$)

d) Vertical force (F_Z)

Fig. 33 Predicted 4/rev vibratory harmonics of hub loads for Metaltail at low-speed flight with $LO = 10\% R$.

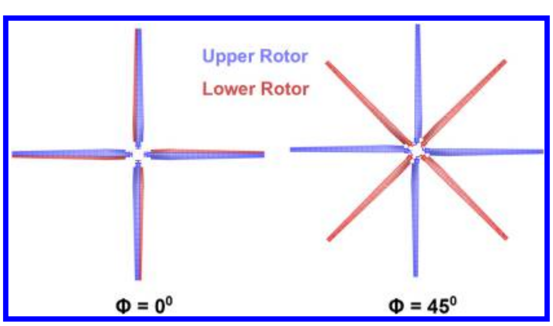

Fig. 34 Coaxial rotor arrangement at $\psi = 0°$ with inter-rotor phase offset $\phi = 0°$ and 45°.

line aerodynamics were discussed, and qualitatively compared with the data published for Sikorsky S-97 Raider aircraft. Predictions of the 3-D stress fields were examined. Although the goal of the paper was capability demonstration, some key conclusions are drawn from the analysis:

1) It is possible to use 3-D structures to model a coaxial rotor and obtain aeroelastic stresses and strains from first principles. This was effectively demonstrated on two notional coaxial model test cases.

2) The open-source verification test cases provide useful templates for 3-D modeling of production rotors from CATIA to stresses/strains.

3) The lower rotor of the coaxial model studied shows higher harmonics in its blade lift distribution due to the wake interactions from the upper rotor at low speeds. The harmonic number depends on the blade twist; a 3/rev was observed in a moderately twisted rotor, and 4/rev for a highly twisted proprotor.

4) The trends obtained for the total main rotor vibratory loads of coaxial Metaltail are found to be consistent with the data published for S-97 Raider. For the range of speeds studied ($\mu \leq 0.25$), the peak vibration for hub moments was observed at the transition speed ($\mu = 0.1$–0.15), and the 4/rev hub vertical force decreased with increasing advance ratio.

5) The effect of the inter-rotor phase (ϕ) on 4P vibratory harmonics showed that $\phi = 0°$ provides lowest 4P vibratory hub moments and $\phi = 45°$ provides lowest 4P vibratory vertical hub force. An ideal choice of phase offset depends on the drop in magnitude of hub loads studied for different phase offsets—the phase offset that provides the maximum drop in hub loads seems a logical choice for reducing overall vibration.

6) The examination of 3-D stress fields revealed that the blade spar takes most of the bending stress with some concentrations near the leading-edge weight. The advancing and retreating sides showed higher stress concentrations over the rotor azimuth. Some localized stress concentrations at the hub were observed, with lower rotor showing slightly higher stresses than the upper rotor.

In summary, the application of 3-D structures for a modern coaxial rotor was demonstrated. This new methodology provides unique capabilities beyond legacy 1D beam-based analysis, such as predicting true 3-D stresses and strains in the rotor and hub components. However, this new capability is worthwhile if it is thoroughly validated. This validation requires a new set of test data that does not exist in the community. There is a need for measured strain data using Digital Image Correlation in wind tunnels and innovative techniques to measure interlaminar strains in rotation at different

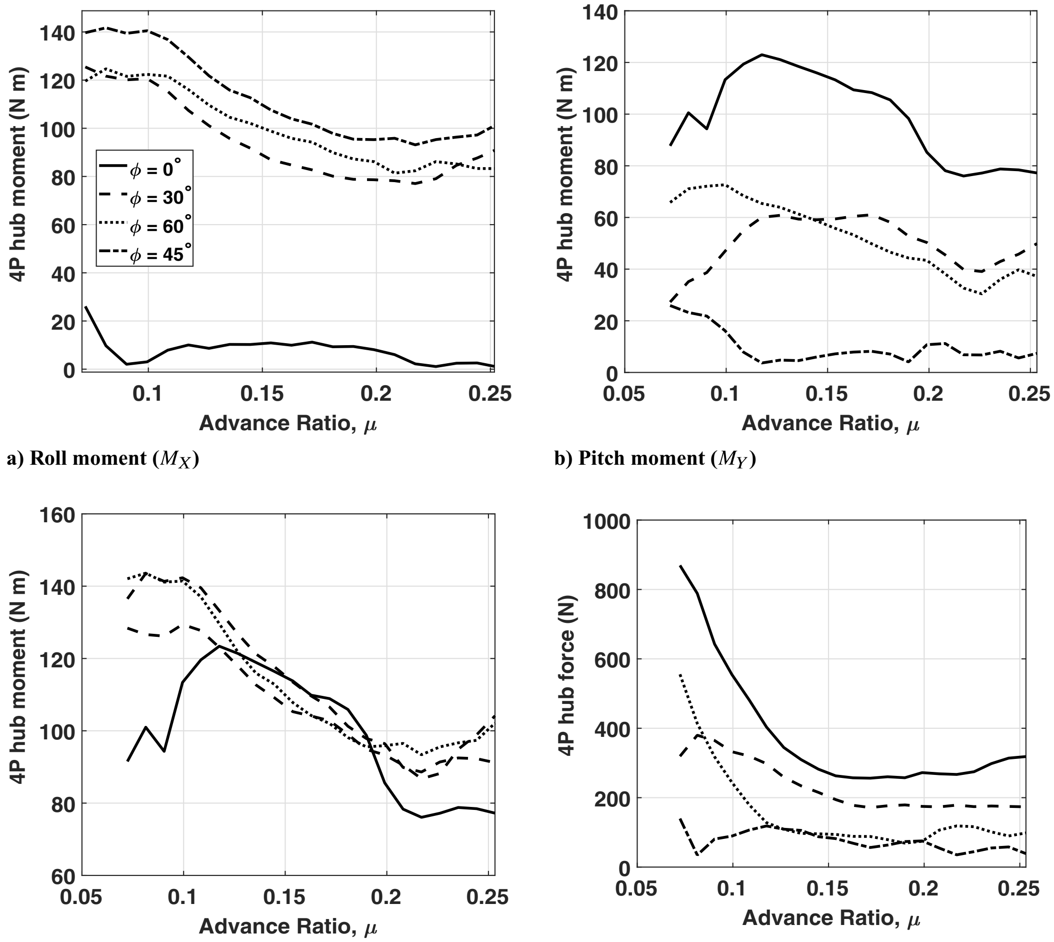

a) Roll moment (M_X)

b) Pitch moment (M_Y)

c) Resultant moment ($\sqrt{M_X^2 + M_Y^2}$)

d) Vertical force (F_Z)

Fig. 35 Total 4/rev vibratory harmonics of Metaltail for different phase offsets at low speeds with $LO = 10\% R$.

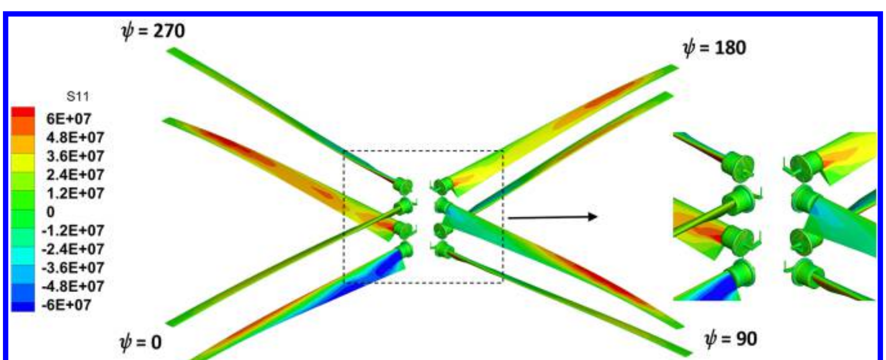

Fig. 36 Axial/bending stress distribution for Metaltail with $LO = 0\% R$.

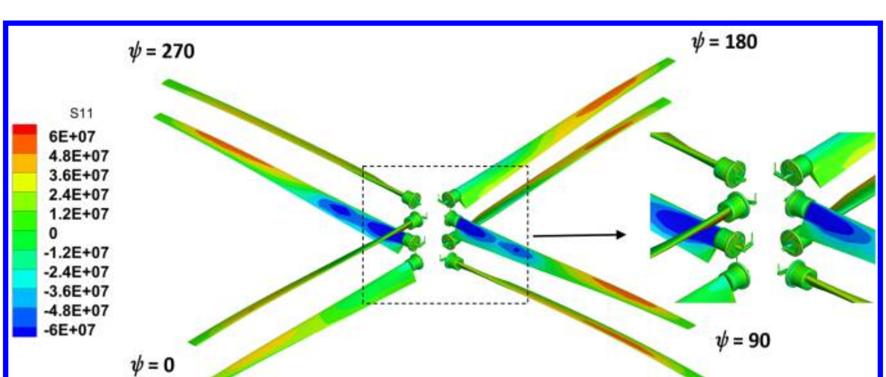

Fig. 37 Axial/bending stress distribution for Metaltail with $LO = 10\% R$.

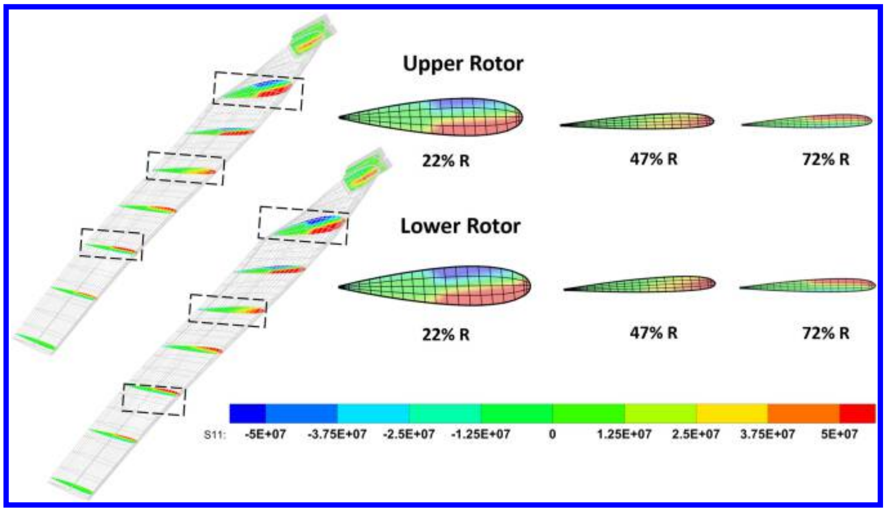

Fig. 38 Blade axial/bending stress distribution at $\psi = 90°$ with $LO = 10\% R$ (scale adjusted).

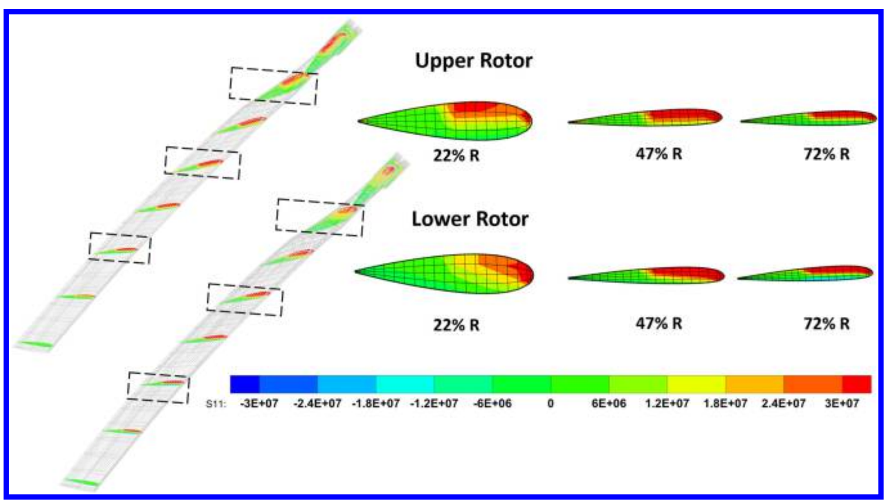

Fig. 39 Blade axial/bending stress distribution at $\psi = 270°$ with $LO = 10\% R$ (scale adjusted).

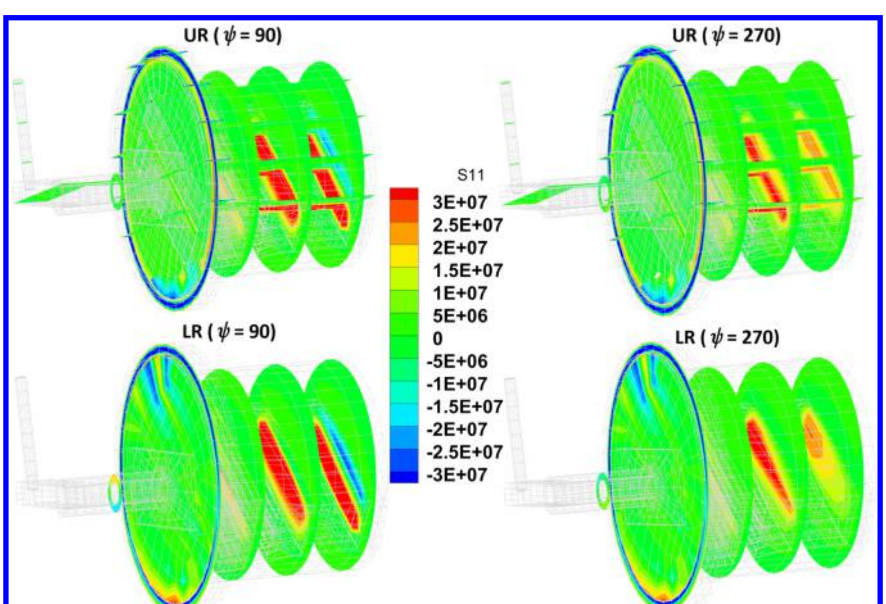

Fig. 40 Axial/bending stress distribution near blade root at $\psi = 90°$ and $270°$ with $LO = 10\% R$.

flight conditions. Hence, research efforts are necessary to obtain such high-quality data for detailed validation. On the analysis end, future work will couple this methodology with CFD to obtain the highest-fidelity solution in structures and aerodynamics.

Acknowledgments

This work was carried out at the Alfred Gessow Rotorcraft Center, University of Maryland at College Park, under the Army/Navy/NASA Vertical Lift Research Center of Excellence (VLRCOE) grant (number W911W61120012), with technical monitoring from Mahendra Bhagwat. We wish to thank the technical points of contact: Wayne Johnson (NASA), Andrew Wissink (Army), and Brahmananda Panda (Boeing).

References

[1] Strawn, R., "High-Performance Computing for Rotorcraft Modeling and Simulation," *Computing in Science and Engineering*, Vol. 12, No. 5, Sept.–Oct. 2010, pp. 27–35.
https://doi.org/10.1109/MCSE.2010.110

[2] Blacker, T., Owen, S., Staten, M., Quadros, R., Hanks, B., Meyers, R., Ernst, C., Merkley, K., Morris, R., and McBride, C., et al., "CUBIT Geometry and Mesh Generation Toolkit 15.2 User Documentation," Sandia National Lab., SAND2016-1649 R, Albuquerque, NM, May 2016.

[3] Rorke, J. B., "Hover Performance Tests of Full Scale Variable Geometry Rotors," NASA CR-2713, Aug. 1976.

[4] Ramasamy, M., "Hover Performance Measurements Toward Understanding Aerodynamic Interference in Coaxial, Tandem, and Tilt Rotors," *Journal of the American Helicopter Society*, Vol. 60, No. 3, July 2015, pp. 1–17.
https://doi.org/10.4050/JAHS.60.032005

[5] Arents, D. N., "An Assessment of the Hover Performance of the XH-59A Advancing Blade Concept Demonstration Helicopter," Eustis Directorate, U.S. Army Air Mobility Research and Development Lab. TR ADA042063, Fort Eustis, VA, 1977.

[6] Ruddell, A. J., "XH-59A ABC Technology Demonstrator Altitude Expansion and Operational Tests," Applied Technology Lab., U.S. Army Research and Technology Laboratories (AVRADCOM) TR ADA111114, Fort Eustis, VA, 1981.

[7] Walsh, D., Weiner, S., Arifian, K., Bagai, A., Lawrence, T., and Blackwell, R., "Development Testing of the Sikorsky X2 Technology Demonstrator," *Proceedings of the American Helicopter Society 65th Annual Forum*, American Helicopter Soc., Fairfax, VA, May 2009.

[8] Walsh, D., Weiner, S., Arifian, K., Lawrence, T., Wilson, M., Millot, T., and Blackwell, R., "High Air-Speed Testing of the Sikorsky X2 Technology Demonstrator," *Proceedings of the American Helicopter Society 67th Annual Forum*, American Helicopter Soc. (now Vertical Flight Soc.), May 2011.

[9] Zhao, J., Brigley, M., and Modarres, R., "S-97 RAIDER Rotor Low Speed Vibratory Loads Analysis Using CFD-CSD," *AIAA SciTech 2019 Forum*, AIAA Paper 2019-0860, Jan. 2019.
https://doi.org/10.2514/6.2019-0860

[10] Zhao, J., Xin, H., Modarres, R., and Brigley, M., "Methodology Correlation for Coaxial Rotor and Blade Load Prediction," *Proceedings of the Vertical Flight Society 76th Annual Forum*, Vertical Flight Soc., Oct. 2020.

[11] Zhao, J., Tuozzo, N., Brigley, M., Modarres, R., Monico, M., and Makinen, S., "CFD-CSD Support for Rotor Design Improvement to Reduce Vibrations," *Proceedings of the Vertical Flight Society 77th Annual Forum*, Vertical Flight Soc., May 2021.

[12] Colemann, C. P., "A Survey of Theoretical and Experimental Coaxial Rotor Aerodynamic Research," NASA TP-3675, 1997.

[13] Escobar, D., Chopra, I., and Datta, A., "High-Fidelity Aeromechanical Analysis of Coaxial Mars Helicopter," *Journal of Aircraft*, Vol. 58, No. 3, May 2021, pp. 609–623.
https://doi.org/10.2514/1.C035895

[14] Ruzicka, G. C., and Strawn, R. C., "Computational Fluid Dynamics Analysis of a Coaxial Rotor Using Overset Grids," *American Helicopter Society Specialist's Conference on Aeromechanics*, American Helicopter Soc. (now Vertical Flight Soc.), Jan. 2008.

[15] Lakshminarayan, V. K., and Baeder, J., "High-Resolution Computational Investigation of Trimmed Coaxial Rotor Aerodynamics in Hover," *Journal of the American Helicopter Society*, Vol. 54, No. 4, Oct. 2009, Paper 042008.
https://doi.org/10.4050/JAHS.54.042008

[16] Juhasz, O., Syal, M., Celi, R., Khromov, V., Rand, O., Ruzicka, G. C., and Strawn, R. C., "Comparison of Three Coaxial Aerodynamic Prediction Methods Including Validation with Model Test Data," *Journal of the American Helicopter Society*, Vol. 59, No. 3, July 2014, pp. 1–14.
https://doi.org/10.4050/JAHS.59.032006

[17] Reed, E., and Egolf, T. A., "Coaxial Rotor Wake and Prop Induction Impact on a Horizontal Tail Using HPCMP CREATE$^{\text{TM}}$-V Helios," *53rd AIAA Aerospace Sciences Meeting*, AIAA Paper 2015-0554, Jan. 2015.
https://doi.org/10.2514/6.2015-0554

[18] Seokkwan, Y., Lee, H. C., and Pulliam, T. H., "Computational Study of Flow Interactions in Coaxial Rotors," *AHS Technical Meeting on Aeromechanics Design for Transformative Vertical Flight*, American Helicopter Soc. (now Vertical Flight Soc.), Jan. 2016.

[19] Barbely, N. L., Komernath, N. M., and Novak, L. A., "A Study of Coaxial Rotor Performance and Flow Field Characteristics," *AHS Technical Conference on Aeromechanics Design for Transformative Vertical Flight*, American Helicopter Soc. (now Vertical Flight Soc.), Jan. 2016.

[20] Johnson, W., "Influence of Lift Offset on Rotorcraft Performance," NASA TP-2009-215404, Nov. 2009.

[21] Yeo, H., and Johnson, W., "Investigation of Maximum Blade Loading Capability of Lift-Offset Rotors," *Journal of the American Helicopter Society*, Vol. 59, No. 1, Jan. 2014, pp. 1–12.
https://doi.org/10.4050/JAHS.59.012005

[22] Schmaus, J., and Chopra, I., "Aeromechanics of Rigid Coaxial Rotor Models for Wind-Tunnel Testing," *Journal of Aircraft*, Vol. 54, No. 4, July 2017, pp. 1486–1497.
https://doi.org/10.2514/1.C034157

[23] Cameron, C., Karpatne, A., and Sirohi, J., "Performance of a Mach-Scale Coaxial Counter-Rotating Rotor in Hover," *Journal of Aircraft*, Vol. 53, No. 3, March 2016, pp. 746–755.
https://doi.org/10.2514/1.C033442

[24] Uehara, D., Sirohi, J., Feil, R., and Rauleder, J., "Blade Passage Loads and Deformation of a Coaxial Rotor System in Hover," *Journal of Aircraft*, Vol. 56, No. 6, Nov. 2019, pp. 2144–2157.
https://doi.org/10.2514/1.C035469

[25] Feil, R., Rauleder, J., Cameron, C., Karpatne, A., and Sirohi, J., "Aeromechanics Analysis of a High-Advance-Ratio Lift-Offset Coaxial Rotor System," *Journal of Aircraft*, Vol. 56, No. 1, Jan. 2019, pp. 166–178.
https://doi.org/10.2514/1.C034748

[26] Feil, R., and Hajek, M., "Aeromechanics of a Coaxial Ultralight Rotorcraft During Turn, Climb, and Descent Flight," *Journal of Aircraft*, Vol. 58, No. 1, Jan. 2021, pp. 43–52.
https://doi.org/10.2514/1.C035684

[27] Ho, J., and Yeo, H., "Rotorcraft Comprehensive Analysis Calculations of a Coaxial Rotor with Lift Offset," *International Journal of Aeronautical and Space Sciences*, Vol. 21, No. 2, June 2020, pp. 418–438.
https://doi.org/10.1007/s42405-019-00221-1

[28] Bagai, A., and Leishman, J. G., "Free-Wake Analysis of Tandem, Tilt-Rotor and Coaxial Rotor Configurations," *Journal of the American Helicopter Society*, Vol. 41, No. 3, July 1996, pp. 196–207.
https://doi.org/10.4050/JAHS.41.196

[29] Syal, M., and Leishman, J. G., "Aerodynamic Optimization Study of a Coaxial Rotor in Hovering Flight," *Journal of the American Helicopter Society*, Vol. 57, No. 4, Oct. 2012, pp. 1–15.
https://doi.org/10.4050/JAHS.57.042003

[30] Brown, R. E., "RotorWake Modeling for Flight Dynamic Simulation of Helicopters," *AIAA Journal*, Vol. 38, No. 1, Jan. 2000, pp. 57–63.
https://doi.org/10.2514/2.922

[31] Singh, P., and Friedmann, P. P., "Application of Vortex Methods to Coaxial Rotor Wake and Load Calculations in Hover," *Journal of Aircraft*, Vol. 55, No. 1, Sept. 2017, pp. 373–381.
https://doi.org/10.2514/1.C034520

[32] Singh, P., and Friedmann, P. P., "Aeromechanics and Aeroelastic Stability of Coaxial Rotors," *Journal of Aircraft*, Vol. 58, No. 6, Nov. 2021, pp. 1386–1405.
https://doi.org/10.2514/1.C036291

[33] Singh, R., Kang, H., Bhagwat, M., Cameron, C., and Sirohi, J., "Computational and Experimental Study of Coaxial Rotor Steady and Vibratory Loads," *AIAA SciTech 2016 Forum*, AIAA Paper 2016-1787, Jan. 2016.
https://doi.org/10.2514/6.2016-1787

[34] Passe, B., Sridharan, A., Baeder, J. D., and Singh, R., "Identification of Rotor-Fuselage Aerodynamic Interactions in a Compound Coaxial Helicopter Using CFD-CSD Coupling," *AHS Technical Conference on Aeromechanics Design for Transformative Vertical Flight*, American Helicopter Soc. (now Vertical Flight Soc.), Jan. 2016.

[35] Klimchenko, V., and Baeder, J. D., "CFD/CSD Study of Interactional Aerodynamics of a Coaxial Compound Helicopter in High-Speed

Forward Flight," *AIAA SciTech 2020 Forum*, AIAA Paper 2020-0304, Jan. 2020.
https://doi.org/10.2514/6.2020-0304

[36] Johnson, W., and Datta, A., "Requirements for Next Generation Comprehensive Analysis of Rotorcraft," *American Helicopter Society Specialist's Conference on Aeromechanics*, American Helicopter Soc. (now Vertical Flight Soc.), Jan. 2008.

[37] Datta, A., "X3D—A 3D Solid Finite Element Multibody Dynamic Analysis for Rotorcraft," *American Helicopter Society Technical Meeting on Aeromechanics Design for Vertical Lift*, Vertical Flight Soc., San Francisco, Jan. 2016.

[38] Patil, M., and Datta, A., "A Scalable Time-Parallel Solution of Periodic Rotor Dynamics in X3D," *Journal of the American Helicopter Society*, Vol. 66, No. 4, Oct. 2021, pp. 1–16.
https://doi.org/10.4050/JAHS.66.042007

[39] Tsai, F., O'Reilly, C., Klimchenko, V., Solomon, E., Phillips, B., Costenoble, A., Chi, C., Govindarajan, B., Nagaraj, V., and Chopra, I., "Metaltail: A Reconfigurable VTOL Aircraft," *Winning Submission to the 35th Annual Vertical Flight Society Student Design Competition, University of Maryland*, Vertical Flight Soc., 2018.

[40] Staruk, W., "CAD-Based Modeling of Advanced Rotary Wing Structures for Integrated 3-D Aeromechanics Analysis," Ph.D. Dissertation, Dept. of Aerospace Engineering, Univ. of Maryland, College Park, 2017, https://drum.lib.umd.edu/handle/1903/20330.

[41] Patil, M., and Datta, A., "Time-Parallel Trim Solution of Helicopter Rotors with Large-Scale 3D Structures," *AIAA SciTech 2021 Forum*, AIAA Paper 2021-1079, Jan. 2021.
https://doi.org/10.2514/6.2021-1079.

[42] Bagai, A., and Leishman, J. G., "Rotor Free-Wake Modeling Using a Pseudo-Implicit Technique—Including Comparisons with Experimental Data," *Journal of the American Helicopter Society*, Vol. 40, No. 3, July 1995, pp. 29–41.
https://doi.org/10.4050/JAHS.40.29

[43] Bagai, A., and Leishman, J. G., "Rotor Free-Wake Modeling Using a Pseudoimplicit Relaxation Algorithm," *Journal of Aircraft*, Vol. 32, No. 6, Nov. 1995, pp. 1276–1285.
https://doi.org/10.2514/3.46875

[44] Bhagwat, M. J., and Leishman, J. G., "Stability Analysis of Helicopter Rotor Wakes in Axial Flight," *Journal of the American Helicopter Society*, Vol. 45, No. 3, July 2000, pp. 165–178.
https://doi.org/10.4050/JAHS.45.165

[45] Bhagwat, M. J., and Leishman, J. G., "Stability, Consistency and Convergence of Time-Marching Free Vortex Rotor Wake Algorithms," *Journal of the American Helicopter Society*, Vol. 46, No. 1, Jan. 2001, pp. 59–71.
https://doi.org/10.4050/JAHS.46.59

[46] Leishman, J. G., Bhagwat, M. J., and Bagai, A., "Free-Vortex Filament Methods for the Analysis of Helicopter Rotor Wakes," *Journal of Aircraft*, Vol. 39, No. 5, Sept. 2002, pp. 59–71.
https://doi.org/10.2514/2.3022

[47] Bhagwat, M. J., and Leishman, J. G., "Rotor Aerodynamics During Maneuvering Flight Using a Time-Accurate Free-Vortex Wake," *Journal of the American Helicopter Society*, Vol. 48, No. 3, July 2003, pp. 143–158.
https://doi.org/10.4050/JAHS.48.143

[48] Ananthan, S., and Leishman, J. G., "Role of Filament Strain in the Free-Vortex Modeling of Rotor Wakes," *Journal of the American Helicopter Society*, Vol. 49, No. 2, April 2004, pp. 176–191.
https://doi.org/10.4050/JAHS.49.176

[49] Shastry, A., and Datta, A., "Predicting Wake and Structural Loads in RPM Controlled Multirotor Aircraft," *Vertical Flight Society Transformative Vertical Flight Technical Meeting*, Vertical Flight Soc., Jan. 2020.

[50] Staruk, W., Datta, A., Chopra, I., and Jayaraman, B., "An Integrated Three-Dimensional Aeromechanics Analysis of the NASA Tilt Rotor Aeroacoustic Model," *Journal of the American Helicopter Society*, Vol. 63, No. 3, July 2018, pp. 1–12.
https://doi.org/10.4050/JAHS.63.032002

[51] Patil, M., and Datta, A., "Three-Dimensional Aeromechanical Analysis of Lift Offset Coaxial Rotors," *AIAA SciTech 2022 Forum*, AIAA Paper 2022-0928, Jan. 2022.
https://doi.org/10.2514/6.2022-0928